# Magnification-driven B-spline Interpolation for Cone Beam Projection and Backprojection

Marion Savanier, Cyril Riddell, Yves Trousset, Emilie Chouzenoux, Jean-Christophe Pesquet

## To cite this version:

Marion Savanier, Cyril Riddell, Yves Trousset, Emilie Chouzenoux, Jean-Christophe Pesquet. Magnification-driven B-spline Interpolation for Cone Beam Projection and Backprojection. Medical Physics : The international journal of medical physics research and practice, In press, 48 (10), ⟨10.1002/mp.15179⟩. ⟨hal-03464469⟩

HAL Id: hal-03464469
https://hal.science/hal-03464469v1

Submitted on 3 Dec 2021

# Magnification-driven B-spline Interpolation for Cone Beam Projection and Backprojection

Marion Savanier$^{(1,2)}$[1], Cyril Riddell$^{(1)}$, Yves Trousset$^{(1)}$, Emilie Chouzenoux$^{(2)}$
and Jean-Christophe Pesquet$^{(2)}$
(1): GE Healthcare, Buc, France
(2): Univ. Paris-Saclay, CentraleSupélec, CVN, Inria, Gif-sur-Yvette, France

**Keywords**: Cone Beam CT, projection, backprojection, B-splines, magnification-driven interpolation, homography

## Abstract

**Purpose:** Discretizing tomographic forward and backward operations is a crucial step in the design of model-based reconstruction algorithms. Standard projectors rely on linear interpolation, whose adjoint introduces discretization errors during backprojection. More advanced techniques are obtained through geometric footprint models that may present a high computational cost and an inner logic that is not suitable for implementation on massively parallel computing architectures. In this work, we take a fresh look at the discretization of resampling transforms and focus on the issue of magnification-induced local sampling variations by introducing a new *magnification-driven* interpolation approach for tomography.
**Methods:** Starting from the existing literature on spline interpolation for magnification purposes, we provide a mathematical formulation for discretizing a one-dimensional homography. We then extend our approach to two-dimensional representations in order to account for the geometry of cone-beam computed tomography with a flat panel detector. Our new method relies on the decomposition of signals onto a space generated by non-uniform B-splines so as to capture the spatially varying magnification that locally affects sampling. We propose various degrees of approximations for a rapid implementation of the proposed approach. Our framework allows us to define a novel family of projector/backprojector pairs parameterized by the order of the employed B-splines. The state-of-the-art distance-driven interpolation appears to fit into this family thus providing new computational layout for this scheme. The question of data resampling at the detector level is handled and integrated with reconstruction in a single framework
**Results:** Results on both synthetic data and real data using a quality assurance phantom, were performed to validate our approach. We show experimentally that our approximate implementations are associated with reduced complexity while achieving a near-optimal performance. In contrast with linear interpolation, B-splines guarantee full usage of all data samples, and thus the X-ray dose, leading to more uniform noise properties. In addition, higher order B-splines allow analytical and iterative reconstruction to reach higher resolution. These benefits appear more significant when downsampling frames acquired by X-ray flat-panel detectors with small pixels.

---

[1] Corresponding author. Contact: marion.savanier@ge.com

**Conclusions:** *Magnification-driven* B-spline interpolation is shown to provide high-accuracy projection operators with good quality adjoints for iterative reconstruction. It equally applies to backprojection for analytical reconstruction and detector data downsampling.

# I. Introduction

Flat-panel based C-arm systems are the most common imaging tools for image-guidance in interventional radiology and surgery. Live 2D imaging and cone-beam computed tomography (CBCT) allow planning, guidance, and control of minimally invasive procedures. C-arm CBCT data differ from that of diagnostic CT. They offer a higher resolution thanks to X-ray flat-panel small pixel pitch. However, the detector low frame rate is a source of angular undersampling when a comparatively high rotation speed is used to minimize the likelihood of patient motion or the amount of injected contrast used to opacify the vessels. The acquisition is largely restricted to the circular orbit, which is another source of undersampling, yielding cone-beam artifacts. Analytical reconstruction is very sensitive to such sampling issues and does not provide as much flexibility to reduce their impact as model-based iterative reconstruction approaches. These approaches are based on a discrete forward projector that captures the geometry of the system to simulate the data formation for any given input volume. This model is then embedded into a cost function, which encodes the statistical properties of the noise affecting the measured data, typically either Poisson or Gaussian. Tomographic reconstruction is an ill-posed problem per se, aggravated by the noise and undersampling in real acquisition systems. A penalization strategy is thus required for better stability, accounting for a priori knowledge about the volume, such as smoothness, edge sparsity, or range constraints. In particular, penalized least squares models have proven useful in CBCT, for instance for tackling noise non-uniformity[1] or undersampling[2].

Powerful algorithms are now available for minimizing penalized least squares cost functions, for a large variety of smooth and nonsmooth convex penalties[3,4,5,6,7]. Most of these algorithms require performing backprojection that matches with the adjoint (i.e., the transpose) the forward projector.

At a first glance, backprojection in model-based iterative reconstruction (MBIR) and backprojection in standard filtered backprojection (FBP) or in the Feldkamp-David-Kress (FDK) method are the same operation. However, when coming to their practical implementation

and discretization, divergent priorities emerge: with FBP, the backprojection operator performs a one-pass operation that must neither introduce artifact nor increase noise nor degrade resolution, and, ideally, be as fast as possible. In contrast, the projector within MBIR aims at describing the data formation precisely. The quality of interpolation increases with redundancy. Convolution by the detector response function degrades resolution, that is then deconvolved during reconstruction. Therefore, backprojection constructed as the transpose of such projector model may neither satisfy the aforementioned FBP constraint, to get the right image in one pass, nor to be quick to compute. To our knowledge, these divergent needs are not satisfied by a single solution in X-ray CT. Linear interpolation for backprojection cannot be ignored, but its transpose appears to underperform as a forward projector. Many different approaches are thus available for the projector. Since X-ray detector bins (or cells) are small surfaces over which the X-ray energy is integrated, and since the volume is reconstructed on a Cartesian grid, state-of-the-art approaches share a geometrical perspective: given a cubic shape for the voxel of the volume, the projective anisotropic footprint of the shape over the detector, and its relation to the detector bin surface, are modeled with respect to the rotation of the system. An important driver for selecting a projector is the model separability. Among all separable footprint models, the distance-driven (DD) offers one of the best compromises between computation cost and image quality for diagnostic CT[8 9].
Time is limited in clinical practice, so a rapid approximate convergence of the early iterations might be more practical than waiting for full convergence, when resorting to MBIR approaches. In this context, there is empirical evidence of models where unmatched projector and backprojector pairs provide significant computation savings at negligible image quality cost with respect to their matched counterparts[10,11,13]. This may come from the fact that the symmetry required by a proper least-squares formulation ensures convergence to a well characterized minimum, but may no longer be optimal in an early stopping scenario: choosing unmatched pairs indeed introduces an additional degree of flexibility since the adjoint only replicates the information included in the forward model. Recently convergence guarantees were recovered in[14] for unmatched pairs in the context of the proximal gradient algorithm.
One essential aspect of the footprint approach is to make explicit assumptions regarding the shape, and therefore size and sampling, of both the volume voxels and the detector bins. These assumptions apply equally to forward or backward projection, yielding symmetry.

This property contrasts with that of models based on linear interpolation, which specify the sampling on either the volume or the detector, but cannot handle both. We advocate here that it is not necessary to use the viewpoint of geometrical discretization to model varying sampling levels: a seminal image resizing algorithm based on the convolution of polynomial B-splines displays this key feature and provides an optimal approximation [15] in terms of $L_2$-norm. This optimality is valid for all B-splines orders, hence even for orders 0 and 1, corresponding to the orders of nearest neighbor and linear interpolations.

As a first contribution, we thus propose a magnification-driven approach to the discretization of cone-beam projection onto a plane based upon projection matrices and extensions of the aforementioned resizing algorithm to homographies. The geometrical assumptions of cubic voxels and square bins are replaced by a continuous model of the sampling variations discretized over the Cartesian grid so that footprints result in one-dimensional convolutions of B-splines. Depending on the order of the B-splines, magnification-driven interpolation provides novel pairs of forward and backward projectors balancing precision and complexity. Our second contribution is to show that the simplest form of such models is actually equivalent to the DD model. This provides new insights on why the DD fits well in X-ray image reconstruction. It also suggests an alternative computation layout that might be better suited to modern highly-parallel processor units. Finally, data resizing, a common step within a detector, prior to performing reconstruction, naturally comes as part of our magnification-driven modeling. Hence our third contribution is to provide alternative computation pipelines for preserving resolution and noise properties at a potentially lower computational cost, for both FBP and MBIR. Our approach is dedicated to the Cartesian grid, for which the sampling rate is not constant by rotation. The proposed magnification-driven interpolation aims to capture all the changes of sampling rates that happen in a tomographic reconstruction. Our approach therefore differs from previous works that introduced smoother isotropic basis functions such as spherically symmetric blobs or multi-dimensional B-splines to reduce or avoid the anisotropy of the sampling[16,17].

The paper is organized as follows. Section II. recalls cone-beam projection on a plane and the B-spline based algorithm for image resizing from which we derive a resampling scheme for tomographic homographies, yielding new discrete projection and backprojection operators based on the convolution of B-splines for either FBP or MBIR. Furthermore, we highlight the relation between state-of-the-art discretizations and our approach. The Section is concluded with the connection between these pairs and existing pre-processing of the data in clinical practice. Experiments on simulated data are presented in Section III. and commented in Section IV. for analytical and iterative reconstruction. An illustration of FDK reconstruction with several interpolation options on a real data case is finally provided. In Section V. we discuss how magnification-driven interpolation sheds light on the current advantages and limitations of standard clinical interpolations and when and how it might better answer specific usage of flat-panel based CBCT.

# II. Method

## II.A. Flat-panel cone-beam geometry

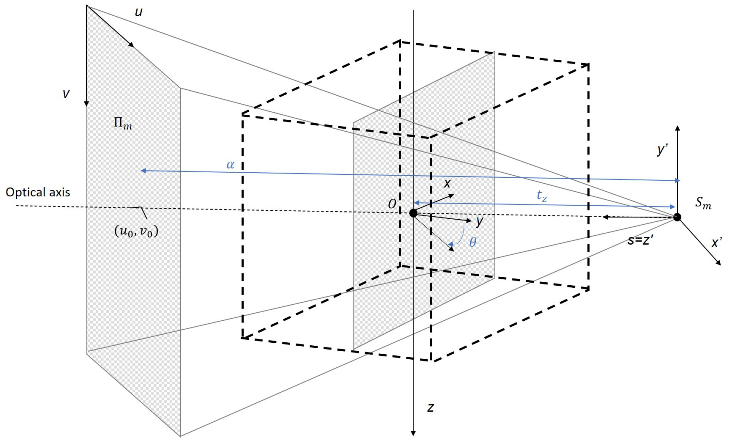

Figure 1: Cone-beam geometry. $(O, x, y, z)$ is the volume coordinate system; $(S_m, x', y', z')$ is the source coordinate system ; $(u, v)$ is the detector plane. Ideal acquisition: $z$, $v$ and $y'$ are aligned.

The projective geometry defines the relationship between voxel coordinates $(x, y, z) \in \mathbb{R}^3$ and the coordinates of the projected pixels $(u, v) \in \mathbb{R}^2$. In X-ray cone beam computed tomography with a flat-panel detector, the data acquisition is characterized by a set of $M \in \mathbb{N}^*$ projection matrices $(\mathbf{P}_m)_{1 \leq m \leq M}$ of size $3 \times 4$, that is one projection matrix per position of the pair X-ray source / detector. For a given projection matrix $\mathbf{P}_m$, coordinates $(u, v)$ of the projection of point $(x, y, z)$ onto the detection plane $\Pi_m$ for the position $S_m$ of the source can be written with homogeneous coordinates $(su, sv, s)$[18] as

$$\left(su, sv, s\right)^\top = \mathbf{P}_m \left(x, y, z, 1\right)^\top . \quad (1)$$

Coordinate $s = 0$ is at the focus point $S_m$ and lies on the so-called optical axis, which is orthogonal to the detector and crosses $S_m$. Point $O$ is the center of the volume and the center of rotation. Projection matrices can be measured very accurately. They provide a precise, compact and indeed powerful way of capturing cone-beam geometry in a continuous space. Axes orientations are shown on Figure 1 as well as an additional intermediate 3D coordinate system $(S_m, x', y', z')$ attached to $S_m$.

Forward projection with one matrix is independent from the other matrices. In contrast, backprojection requires the $M$ projected images as it is the sum over $m \in \{1, \ldots, M\}$ of the backprojection of each single projected image obtained using matrix $\mathbf{P}_m$. For every $m$, the only common condition we set, pertaining to tomography, is that the projection matrices operate on the same coordinate system $(O, x, y, z)$ such that $z$ is an axis of rotation always aligned with the axis $v$ of the detector. That being said, we can focus the discussion on a single matrix and drop index $m$.

Any projection matrix $\mathbf{P} = (p_{i,j})_{1 \leq i \leq 3, 1 \leq j \leq 4}$ can be decomposed into the product of a matrix $\mathbf{P}_\mathrm{i}$ of intrinsic parameters relating $(x', y', z')$ to $(u, v)$ and matrix $\mathbf{P}_\mathrm{e}$ of extrinsic parameters relating $(x, y, z)$ to $(x', y', z')$[19]. Matrix $\mathbf{P}_\mathrm{i}$ is defined by

$$\mathbf{P}_\mathrm{i} = \begin{pmatrix} \alpha & 0 & u_0 \\ 0 & -\alpha & v_0 \\ 0 & 0 & 1 \end{pmatrix} \tag{2}$$

where $\alpha$ is the source-to-detector distance in unit of pixel size and $(u_0, v_0)$ are the coordinates of the orthogonal projection of point $S$ over the detector, also called the piercing point where the optical axis crosses the detector plane. Here again, the unit of length is the pixel size, which is given with the data at backprojection, while it is a parameter for projection. Matrix $\mathbf{P}_\mathrm{e}$ is a 3D rotation and translation operator that, given our specified tomographic conditions, is given by

$$\mathbf{P}_\mathrm{e} = \begin{pmatrix} \cos\theta & \sin\theta & 0 & t_x \\ 0 & 0 & -1 & t_y \\ -\sin\theta & \cos\theta & 0 & t_z \end{pmatrix}, \tag{3}$$

where $\theta$ is the rotation angle within plane $(x, y)$, $(t_x, t_y)$ are translations that, when not equal to 0, capture a centering shift of the detector, and $t_z$ is the distance from source $S$ to origin $O$ which is also set as the center of rotation. The unit of length is the voxel size, which is a parameter at backprojection, while it is given with the volume at projection. The optical axis is positioned at angle $\theta + \pi$ in this configuration. It follows that $\mathbf{P}$ has two null coefficients:

$$\mathbf{P} = \mathbf{P}_{\mathrm{i}}\mathbf{P}_{\mathrm{e}} = \begin{pmatrix} p_{1,1} & p_{1,2} & 0 & p_{1,4} \\ p_{2,1} & p_{2,2} & p_{2,3} & p_{2,4} \\ p_{3,1} & p_{3,2} & 0 & p_{3,4} \end{pmatrix}. \tag{4}$$

Matrix $\mathbf{P}$ provides direct access to key parameters since $p_{3,1} = -\sin\theta$, $p_{3,2} = \cos\theta$, $p_{3,4} = t_z$, and $p_{2,3} = \alpha$. However, it does not give access to the voxel and pixel units of length, but only to their ratio given by $\alpha/t_z$, i.e. the magnification factor at the origin $O$. This ratio is used as a reference. Projection operations are performed at equivalent sampling for a ratio of 1 (called isosampling). A ratio greater than 1 oversamples the detector side or undersamples the volume side, and inversely for a ratio lower than 1.

## II.B. Forward and backward cone-beam projection based on convolved B-splines

### II.B.1. Projection as a sum of 2D homographies

Discretization over the Cartesian grid will here mean decomposing the cone-beam projection of a volume into the weighted sum along one axis of the projection of each volume plane orthogonal to said axis. Each projection is thus turned into a homography. More precisely, when $|\cos\theta| > |\sin\theta|$, we use axis $y$ that is closest to the optical axis, otherwise axis $x$ is used. This ensures that all homographies are invertible. Without loss of generality, we now consider that $t_x = t_y = 0$ as these translations do not change the sampling issues. Let us consider a summation along axis $y$: coordinates $(u, v)$ of the projection of any point $(x, y_0, z)$ of the volume coronal plane $y = y_0$ onto the detector plane are given by

$$\left(su, sv, s\right)^\top = \mathbf{P}\left(x, y_0, z, 1\right)^\top = \mathbf{H}_{y_0}\left(x, z, 1\right)^\top \tag{5}$$

with $\mathbf{H}_{y_0} = \begin{pmatrix} p_{1,1} & 0 & p_{1,2}y_0 + p_{1,4} \\ p_{2,1} & p_{2,3} & p_{2,2}y_0 + p_{2,4} \\ p_{3,1} & 0 & p_{3,2}y_0 + p_{3,4} \end{pmatrix} = \begin{pmatrix} h_{1,1} & 0 & h_{1,3} \\ h_{2,1} & h_{2,2} & h_{2,3} \\ h_{3,1} & 0 & h_{3,3} \end{pmatrix}$,

so that

$$\left\{ \begin{array}{rcl} s(x) & = & h_{3,1}x + h_{3,3} \\ u & = & h_1(x) = \frac{h_{1,1}x + h_{1,3}}{s(x)} \\ v & = & h_2(x, z) = \frac{h_{2,1}x + h_{2,2}z + h_{2,3}}{s(x)}. \end{array} \right. \tag{6}$$

The projection of plane $y = y_0$ is thus a resampling by 2D homography $\mathbf{H}_{y_0}$ which, in our tomographic case, displays a resampling in $v$ that is a 1D magnification between $v$ and $z$ of factor $h_{2,2}/s(x)$.

The resampling in $u$ is a 1D homography of $x$ only. This 1D resampling function corresponds to a flat-detector fan-beam geometry. In the following, we shall thus recast the discretization of a flat panel fan-beam homographic resampling as a generalization of a 1D resampling pipeline with constant magnification using the convolution of B-splines.

### II.B.2. Resampling algorithm for a constant magnification

Let $\Delta > 0$ and let $a(\Delta\cdot)$ be the continuous magnified version of a 1D continuous signal $a : \mathbb{R} \to \mathbb{R}$. The resampling task consists in computing from $N_I$ uniformly spaced samples of $a$ with sampling step 1, $N_J$ samples that are therefore uniformly spaced by $\Delta$. A resampling step $\Delta > 1$ thus corresponds to a downsampling (reduction) while a sampling step $\Delta < 1$ is an upsampling (enlargement), the magnification factor being equal to $1/\Delta$. We denote $I = \{1, \ldots, N_I\}$ and $J = \{1, \ldots, N_J\}$ the respective sets of indices. In[15], the authors proposed a resampling algorithm to minimize information loss when computing a reduction/enlargement $a_\Delta$ on the same axis as $a$ from the vector $\mathbf{a} \in \mathbb{R}^{N_J}$ of known values $(a(j))_{j\in J}$ of $a : \mathbb{R} \to \mathbb{R}$ using B-splines expansions. The central B-spline of order $n \in \mathbb{N}$ is denoted by $\beta^n : \mathbb{R} \to \mathbb{R}$. The convolution product is $(f * g)(\cdot) = \int_{-\infty}^{+\infty} f(t)g(\cdot - t)dt$ for functions $f$ and $g$ in $L^2(\mathbb{R})$, the Hilbert space of measurable, square-integrable functions from $\mathbb{R}$ to $\mathbb{R}$. The convolution product is also defined for discrete signals $a \in \ell_2$ and $b \in \ell_1$ as, for $k \in \mathbb{Z}$, $(b * a)(k) = \sum_{\ell\in\mathbb{Z}} b(\ell)a(k - \ell)$ where $\ell_2$ (resp. $\ell_1$) is the space of square summable (resp. summable) sequences. Let us define $b^n \in \mathbb{R}^{\mathbb{Z}}$ as the discrete B-spline of order $n$, obtained by sampling $\beta^n$ at integer values, i.e. $b^n(\ell) = \beta^n(\ell)$ for $\ell \in \mathbb{Z}$.

Given values $(a(j))_{j\in J}$, we will assume that the continuous signal $a$ can be represented in the space spanned by $\{\beta^n(\cdot - j) \mid j \in J\}$ by expansion

$$a(x) = \sum_{j\in J} c(j)\beta^n(x - j), \tag{7}$$

where $\mathbf{c} = (c(j))_{j\in J} \in \mathbb{R}^{N_J}$ is the associated set of B-spline coefficients of $a$ such that

$$(\forall j \in J) \quad a(j) = (b^n * c)(j) = \sum_{\ell\in\mathbb{Z}} b^n(\ell)c(j - \ell). \tag{8}$$

The magnification of the centered B-spline of order $n$ is defined by $\beta^n_\Delta = \beta^n(\cdot/\Delta)$ and, most importantly, is itself a centered B-spline of order $n$. It provides a representation $a_\Delta$ onto the space spanned by functions $\{\beta^n_\Delta(\cdot - \Delta i) \mid i \in I\}$ given by

$$a_\Delta(x) = \sum_{i \in I} c_\Delta(i)\beta^n_\Delta(x - \Delta i). \tag{9}$$

The vector of coefficients $\mathbf{c}_{\boldsymbol{\Delta}} = (c_\Delta(i))_{i \in I} \in \mathbb{R}^{N_I}$ is determined by minimizing the norm $\|a_\Delta - a\|_{L^2(\mathbb{R})}$ and thus satisfies normal equations[21], which are expressed in matrix form as

$$\mathbf{T}\mathbf{c}_{\boldsymbol{\Delta}} = \boldsymbol{\Xi}\mathbf{c}, \tag{10}$$

where $\boldsymbol{\Xi} = (\Xi_{i,j})_{(i,j) \in I \times J} \in [0, +\infty[^{N_I \times N_J}$ and $\mathbf{T} = (T_{i,i'})_{(i,i') \in I^2} \in [0, +\infty[^{N_I \times N_I}$ are such that,[2]

$$\Xi_{i,j} = \int_{-\infty}^{+\infty} \beta^n(x - j)\beta^n_\Delta(x - \Delta i)dx = \xi^{n,n}_\Delta(j - \Delta i) \tag{11}$$

with, for every $\theta \in \mathbb{R}$,

$$\xi^{n,n}_\Delta(\theta) = (\beta^n * \beta^n_\Delta)(\theta) \tag{12}$$

and, for every $(i, i') \in I^2$,

$$T_{i,i'} = \int_{-\infty}^{+\infty} \beta^n_\Delta(x - \Delta i)\beta^n_\Delta(x - \Delta i')dx = \beta^{2n+1}_\Delta((i - i')\Delta) = b^{2n+1}(i - i'). \tag{13}$$

$\boldsymbol{\Xi}$ is a cross-correlation matrix containing the correlations of functions $\beta^n_\Delta$ and $\beta^n$ according to the relative positions of the samples. In our context of projective geometry, these cross-correlations will be interpreted as "footprints". Note that the general scaling property of the convolution of B-splines implies that

$$(\forall \theta \in \mathbb{R}) \quad \xi^{n,n}_\Delta(\theta) = \Delta \xi^{n,n}_{\frac{1}{\Delta}}(\theta/\Delta). \tag{14}$$

Therefore, the magnification of step $\Delta$ and the inverse magnification of step $1/\Delta$ result in the same footprint, up to a normalization factor.

Matrix $\mathbf{T}$ is a Gram matrix, hence symmetric and semi-definite positive, independent of $\Delta$. It is also Tœplitz so that its inverse can be implemented by means of digital filters. Finally, $\mathbf{a}_{\boldsymbol{\Delta}}$ is given by

$$\mathbf{a}_{\boldsymbol{\Delta}} = \boldsymbol{\Lambda}\mathbf{T}^{-1}\boldsymbol{\Xi}\mathbf{c}, \tag{15}$$

where $\boldsymbol{\Lambda} = (\Lambda_{i,i'})_{(i,i') \in I^2}$ is such that,

$$(\forall (i, i') \in I^2) \quad \Lambda_{i,i'} = b^n(i - i'). \tag{16}$$

---

[2] The functions $\beta^n$ with $n \in \mathbb{N}$ are even.

The discrete convolution form of (15) is

$$(\forall i \in I) \quad a_{\Delta}^{n}(i) = \left(b^n * (b^{2n+1})^{-1} * (\boldsymbol{\Xi}\mathbf{c})\right)(i). \tag{17}$$

This routine can be directly applied to image magnification by implementing separable magnifications along each direction resulting in successive 1D processing along the rows and the columns of an image.

In the following, we propose to extend this approach for dealing with general homographies, by allowing the signal of known samples to be approximated with B-splines of order $m$, possibly different from the order $n$ of the output.

### II.B.3. Magnification-driven resampling algorithm for a 1D homography

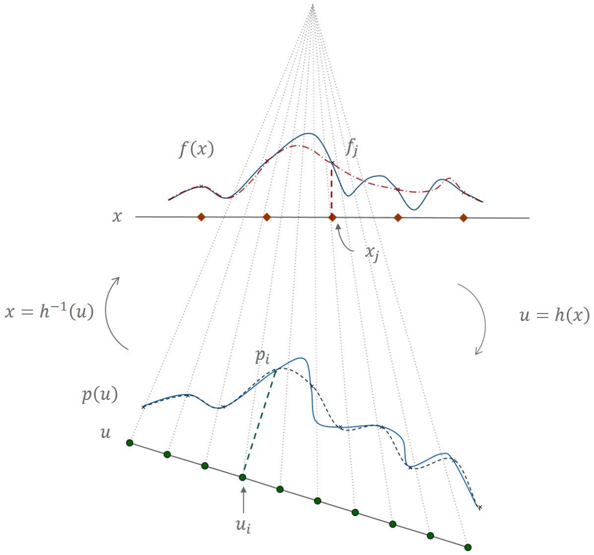

Figure 2: Example of a signal (solid line) and its B-splines approximations in the volume and in the projections (dashed line).

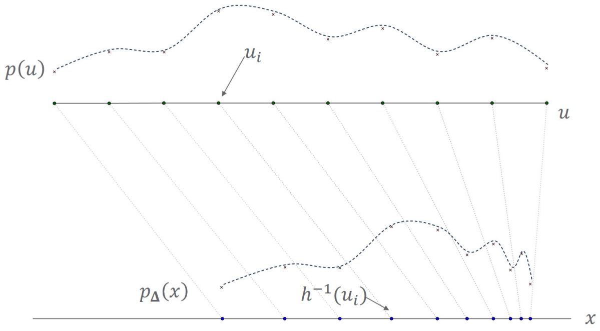

Figure 3: Construction of $p_{\boldsymbol{\Delta}}(x)$ from $p(u)$ on the same axis as $f(x)$.

We now consider that one line $f(x)$ of the volume and one line of the projector $p(u)$ are related by the 1D homography $h$ such that, for every $x \in \mathcal{X} = ]-h_{3,3}/h_{3,1}, +\infty[$,

$$u = h(x) = \frac{h_{1,1}x + h_{1,3}}{h_{3,1}x + h_{3,3}}. \tag{18}$$

This defines a bijective mapping from $\mathcal{X}$ to $\mathcal{U} = h(\mathcal{X})$. Backprojection generates $f$ from $p$ and projection generates $p$ from $f$, as shown in Figure 2, according to

$$p(u) = p \circ h(x) = \frac{f(x)}{|h'(x)|}, \tag{19}$$

or

$$f(x) = f \circ h^{-1}(u) = |h'(h^{-1}(u))| p(u), \tag{20}$$

where $h'$ denotes the derivative of $h$. These relations ensure the expected conservation of matter density through the integral identity:

$$\int_{\mathcal{U}} p(u) du = \int_{\mathcal{X}} f(x) dx. \tag{21}$$

Let $N_I$ (resp. $N_J$) be the number of samples along $u$ (resp. $x$) and let $I = \{1, \dots, N_I\}$ (resp. $J = \{1, \dots, N_J\}$) be the associated set of indices. Let $(u_i)_{i \in I}$ be the locations of values $(p_i)_{i \in I}$ of discrete signal $\mathbf{p} = (p(u_i))_{i \in I}$. Let $(x_j)_{j \in J}$ be the locations of the observed values $(f_j)_{j \in J}$ of $f$, giving rise to the discrete signal $\mathbf{f} = (f(x_j))_{j \in J}$. As an extension of (14), let us define function $\xi_{\Delta}^{m,n}$ such that

$$(\forall \theta \in \mathbb{R}) \quad \xi_{\Delta}^{m,n}(\theta) = \beta^m * \beta_{\Delta}^n(\theta). \tag{22}$$

The goal of the projection step is to compute samples $(p_i)_{i \in I}$ from samples $(f_j)_{j \in J}$.
We first assume that $f$ belongs to the space spanned by $\{\beta^m(\cdot - x_j) \mid j \in J\}$ i.e.,

$$f(x) = \sum_{j \in J} c(j) \beta^m(x - x_j), \tag{23}$$

where $\mathbf{c} = (c(j))_{j \in J}$ is the associated set of B-spline coefficients of $f$.
Unlike the magnification case, the homography of a centered B-spline is not a B-spline in general. The magnification-driven approach consists therefore in approximating the homography of the centered B-spline by its magnification. We thus use the absolute value $|h'(x)|$ of the derivative of $h$ at $x$, that provides the continuous change in sampling rate from $x$ to $u$ induced by $h$. Furthermore, we note that $|(h^{-1})'(u)| = 1/|h'(x)|$. For the approximation to be valid, coefficient $h_{3,1}$ must be small enough to make the variation of the magnification factor

negligible over the support of the B-splines. We have then $|(h^{-1})'(z)| \simeq 1/|h'(z)| \simeq h_{1,1}/h_{3,3}$. Let $\Delta_i = 1/|h'(h^{-1}(u_i))|$ be the local sampling step in an open neighborhood $\mathcal{V}(u_i)$ of $u_i$ with $i \in I$. This defines a vector of resampling parameters $\boldsymbol{\Delta} = (\Delta_i)_{i\in I}$. Hence, when $u \in \mathcal{V}(u_i)$, (20) yields

$$p(u) = \frac{f(h^{-1}(u))}{|h'(h^{-1}(u))|} \simeq \Delta_i f(h^{-1}(u)). \tag{24}$$

Let $p_{\boldsymbol{\Delta}}$ be an approximation of $p$ on the same axis as $f$ such that, for every $i \in I$,

$$p(u_i) = \Delta_i\, p_{\boldsymbol{\Delta}}(h^{-1}(u_i)) \tag{25}$$

(see Figure 3). We make the assumption that $p_{\boldsymbol{\Delta}}$ can be decomposed onto a family of nonuniform B-splines of order $n \in \mathbb{N}$ as

$$p_{\boldsymbol{\Delta}}(x) = \sum_{i\in I} s_{\Delta_i}(i)\, \beta^n_{\Delta_i}(x - h^{-1}(u_i)). \tag{26}$$

The optimal coefficients $\mathbf{s}^*_{\boldsymbol{\Delta}} = (s_{\Delta_i}(i))_{i\in I}$ satisfy the normal equations according to

$$\mathbf{G}\mathbf{s}^*_{\boldsymbol{\Delta}} = \mathbf{F}\mathbf{c}, \tag{27}$$

where $\mathbf{F} = (F_{i,j})_{(i,j)\in I\times J} \in [0,+\infty[^{N_I\times N_J}$ and $\mathbf{G} = (G_{i,l})_{(i,l)\in I^2} \in [0,+\infty[^{N_I\times N_I}$ are such that, for every $(i,l) \in I^2$ and $j \in J$,

$$F_{i,j} = \int_{-\infty}^{+\infty} \beta^m(x - x_j)\beta^n_{\Delta_i}(x - h^{-1}(u_i))dx = \xi^{m,n}_{\Delta_i}(x_j - h^{-1}(u_i)) \tag{28}$$

and

$$\begin{aligned} G_{i,l} &= \int_{-\infty}^{+\infty} \beta^n_{\Delta_l}(x - h^{-1}(u_l))\beta^n_{\Delta_i}(x - h^{-1}(u_i))dx = \beta^n_{\Delta_l} * \beta^n_{\Delta_i}(h^{-1}(u_l) - h^{-1}(u_i)) \\ &= \Delta_i \xi^{n,n}_{\Delta_l/\Delta_i}\left(\frac{h^{-1}(u_l) - h^{-1}(u_i)}{\Delta_i}\right) = \Delta_l \xi^{n,n}_{\Delta_i/\Delta_l}\left(\frac{h^{-1}(u_i) - h^{-1}(u_l)}{\Delta_l}\right). \end{aligned} \tag{29}$$

$\mathbf{F}$ contains the footprints of functions $(\beta^n_{\Delta_i}(\cdot - h^{-1}(u_i)))_{i\in I}$ and (resp. over) $(\beta^m(\cdot - x_j))_{j\in J}$ (see Figure 4). Note that the Gram matrix $\mathbf{G}$ is not Tœplitz anymore and that its diagonal elements are

$$(\forall i \in I) \quad G_{i,i} = \Delta_i \xi^{n,n}_1(0) = \Delta_i b^{2n+1}(0). \tag{30}$$

Finally the expression of vector $\mathbf{p}$ is derived from (25):

$$\mathbf{p} = \mathrm{Diag}(\boldsymbol{\Delta})\tilde{\boldsymbol{\Lambda}}\mathbf{s}^*_{\boldsymbol{\Delta}} \tag{31}$$

where $\mathrm{Diag}(\boldsymbol{\Delta})$ is the diagonal matrix whose diagonal is equal to vector $\boldsymbol{\Delta}$ and $\tilde{\boldsymbol{\Lambda}} = (\tilde{\Lambda}_{i,l})_{(i,l)\in I^2} \in [0,+\infty[^{N_I \times N_I}$ is such that,

$$\tilde{\Lambda}_{i,l} = \beta^n_{\Delta_i}\left(h^{-1}(u_l) - h^{-1}(u_i)\right). \tag{32}$$

By combining (27) and (31), we have

$$\mathbf{p} = \mathrm{Diag}(\boldsymbol{\Delta})\tilde{\boldsymbol{\Lambda}}\mathbf{G}^{-1}\mathbf{F}\mathbf{c}, \tag{33}$$

where $\mathbf{G}^{-1}$ denotes the pseudo-inverse of $\mathbf{G}$. Note that the above equality holds exactly provided that model (23)-(26) is perfectly satisfied, which is obviously an approximation in practice.

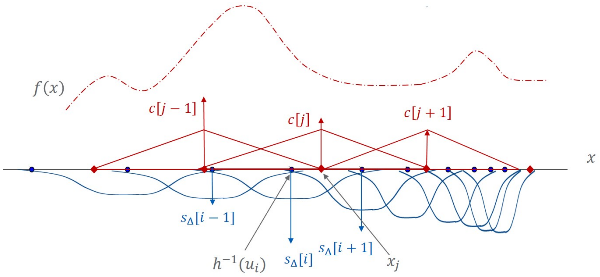

Figure 4: Least-square resampling of $f(x)$ on a basis of non-uniform B-splines centered on $(h^{-1}(u_i))_{i\in I}$.

Let us now see how to retrieve $\mathbf{f}$ from $\mathbf{p}$ in the backprojection stage. Symmetrically, we assume that the continuous projection $p$ can be decomposed as

$$p(u) = \sum_{i\in I} c'(i)\beta^n(u - u_i), \tag{34}$$

where $\mathbf{c}' = (c'(i))_{i\in I}$ is the associated set of B-spline coefficients. A new vector of resampling parameters $\boldsymbol{\Delta'} = (\Delta'_j)_{j\in J}$ is defined such that $\Delta'_j = |h'(x_j)|$, the sampling step in $\mathcal{V}(x_j)$, an open neighborhood of $x_j$. Thus,

$$f(x_j) = |h'(x_j)|p(h(x_j)) = \Delta'_j\, p(h(x_j)). \tag{35}$$

Let $f_{\boldsymbol{\Delta'}}$ be an approximation of $f$ on the same axis as $p$ and such that, for every $j \in J$,

$$f(x_j) = \Delta'_j f_{\boldsymbol{\Delta'}}(h(x_j)). \tag{36}$$

We now assume that $f_{\boldsymbol{\Delta'}}$ is the projection of $p$ onto the vector space generated by $\{\beta^m_{\Delta_j}(\cdot - h(x_j)) \mid j \in J\}$, which leads to the following relation:

$$\mathbf{f} = \mathrm{Diag}(\boldsymbol{\Delta'})\tilde{\boldsymbol{\Lambda}}'(\mathbf{G}')^{-1}\mathbf{F}'\mathbf{c}', \tag{37}$$

where matrices $\mathbf{F}' \in [0,+\infty[^{N_J \times N_I}$, $\mathbf{G}' \in [0,+\infty[^{N_J \times N_J}$, and $\tilde{\mathbf{\Lambda}}' \in [0,+\infty[^{N_J \times N_J}$ are such that, for every $(j,l) \in J^2$ and $i \in I$,

$$F'_{j,i} = \xi^{n,m}_{\Delta'_j}(u_i - h(x_j)), \quad G'_{j,l} = \Delta'_j \xi^{m,m}_{\Delta'_l/\Delta'_j}\left(\frac{h(x_l) - h(x_j)}{\Delta'_j}\right), \quad \tilde{\Lambda}'_{j,l} = \beta^m_{\Delta'_l}\left(h(x_l) - h(x_j)\right). \tag{38}$$

**Remark 1** *For every $(n,m) \in \mathbb{N}^2$, the support of $\beta^n_\Delta$ is $]-(n+1)\Delta/2, (n+1)\Delta/2[$ and, for every $\Delta > 0$ the support of function $\xi^{m,n}_\Delta$ is thus equal to $]-(m+1+(n+1)\Delta)/2, (m+1+(n+1)\Delta)/2[$. This implies that most elements of matrices $\mathbf{G}$, $\mathbf{F}$, $\tilde{\mathbf{\Lambda}}$, $\mathbf{G}'$, $\mathbf{F}'$, and $\tilde{\mathbf{\Lambda}}'$ are zero, giving them a band structure. For example, according to (29), for every $(i,l) \in I^2$, if*

$$|h^{-1}(u_l) - h^{-1}(u_i)| \geq (n+1)\frac{\Delta_i + \Delta_l}{2}, \tag{39}$$

*then $G_{i,l} = 0$ and, if*

$$|h^{-1}(u_l) - h^{-1}(u_i)| \geq (n+1)\frac{\Delta_i}{2}, \tag{40}$$

*then $\tilde{\Lambda}_{i,l} = 0$.*

**Approximation for low-order splines:** In order to reduce the computation burden related to the inversion of matrix $\mathbf{G}$, we propose to approximate this matrix by a surrogate matrix $\tilde{\mathbf{G}} \in \mathbb{R}^{N_I \times N_I}$ in (33).

For every $(i,l) \in I^2$ for which (39) is not satisfied, we will make the assumption that

$$h^{-1}(u_l) \simeq h^{-1}(u_i) + \frac{1}{h'(h^{-1}(u_i))}(u_l - u_i) = h^{-1}(u_i) \pm \Delta_i(l-i). \tag{41}$$

Based on these approximations, (29), and Remark 1, we will define $\tilde{\mathbf{G}} = (\tilde{G}_{i,l})_{(i,l)\in I^2}$ as follows:

- if $|u_l - u_i| \leq n$, then

$$\tilde{G}_{i,l} = \sqrt{\Delta_i \Delta_l}\,\xi^{n,n}_1(l-i) = \sqrt{\Delta_i \Delta_l}\,b^{2n+1}(l-i), \tag{42}$$

- otherwise $\tilde{G}_{i,l} = 0$.

In particular, $\tilde{G}_{i,i} = G_{i,i}$ and we can write $\tilde{\mathbf{G}} = \operatorname{Diag}(\mathbf{\Delta})^{1/2}\mathbf{T}_n \operatorname{Diag}(\mathbf{\Delta})^{1/2}$ where $\mathbf{T}_n$ is the Tœplitz matrix previously encountered for the magnification case with B-splines of order $n$. The resulting approximate vector of B-spline coefficients then reads as

$$\tilde{\mathbf{s}}^*_{\mathbf{\Delta}} = \operatorname{Diag}(\mathbf{\Delta})^{-1/2}\mathbf{T}_n^{-1} \operatorname{Diag}(\mathbf{\Delta})^{-1/2}\mathbf{F}\mathbf{c}. \tag{43}$$

**Remark 2** i) *Since multiplication by a Tœplitz matrix is equivalent to discrete convolution with suitable boundary conditions, the components* $(\tilde{s}^*_{\mathbf{\Delta},i})_{i\in I}$ *of vector* $\tilde{s}^*_{\mathbf{\Delta}}$ *are given by*

$$(\forall i \in I) \quad \tilde{s}^*_{\mathbf{\Delta},i} = \frac{1}{\sqrt{\Delta_i}} \sum_{l=1}^{N_I} \frac{1}{\sqrt{\Delta_l}} (\mathbf{Fc})_l \, (b^{2n+1})^{-1}(i-l), \tag{44}$$

*where*

$$(\forall l \in I) \quad (\mathbf{Fc})_l = \sum_{j=1}^{N_J} c(j) \, \xi^{m,n}_{\Delta_i}(h^{-1}(u_l) - x_j). \tag{45}$$

ii) *Applying* (41) *for every couple* $(i,l) \in I^2$ *that does not satisfy* (39) *and using* (32), *leads to a rougher approximation where* $\tilde{\mathbf{\Lambda}}$ *is replaced by* $\mathbf{\Lambda}$, *which was also introduced in the magnification case with B-splines of order* $n$. *Here again,* $\Lambda_{i,i} = \tilde{\Lambda}_{i,i}$.

*Then, the components of vector* $\mathbf{p}$ *in* (33) *are approximated by the following discrete convolution*

$$(\forall i \in I) \quad \tilde{p}_i = \Delta_i \, (b^n * \tilde{s}^*_{\mathbf{\Delta}})(i). \tag{46}$$

The same simplifications apply for backprojection: we define surrogate matrix $\tilde{\mathbf{G}}' \in \mathbb{R}^{N_J \times N_J}$ such that, for $(j,l) \in J^2$ such that $|x_l - x_j| \leq m$,

$$\tilde{G'}_{j,l} = \sqrt{\Delta'_j \Delta'_l} \, b^{2m+1}(l-j). \tag{47}$$

As above, vector $\mathbf{f}$ in (37) can be approximated by

$$\tilde{\mathbf{f}} = \mathrm{Diag}(\mathbf{\Delta'}) \tilde{\mathbf{\Lambda}}' \, \mathrm{Diag}(\mathbf{\Delta'})^{-1/2} \mathbf{T}_m^{-1} \, \mathrm{Diag}(\mathbf{\Delta'})^{-1/2} \mathbf{F}'\mathbf{c}', \tag{48}$$

where the inversion performed by $\mathbf{T}_m^{-1}$ can be implemented by filtering with $(b^{2m+1})^{-1}$.

**Remark 3**

i) *When comparing Equations* (33) *and* (37), *we note that the main modeling difference lies in the set of magnification factors. Given the scaling property*

$$(\forall \theta \in \mathbb{R}) \quad (1/\Delta) \xi^{m,n}_{\Delta}(\theta) = \xi^{n,m}_{1/\Delta}(\theta/\Delta), \tag{49}$$

*we remark that*

$$F'_{i,j} = \xi^{n,m}_{\Delta'_j}(h(x_j) - u_i) = \Delta'_j \xi^{m,n}_{1/\Delta'_j}((h(x_j) - u_i)/\Delta'_j). \tag{50}$$

*If $u_i \simeq h(x_j)$ with $j \in J$ (with $N_J \leq N_I$), then*

$$\Delta'_j \simeq \frac{1}{\Delta_i}. \tag{51}$$

*This means that one could use the sampling steps $\mathbf{\Delta}^{-1} = (1/\Delta_j)_{j \in J}$ instead of $\mathbf{\Delta'}$ and thus, according to (49), (28), and (38),*

$$\begin{aligned} F'_{j,i} = \frac{1}{\Delta_i} \xi^{m,n}_{\Delta_i}\big(\Delta_i(h(x_j) - u_i)\big) &\simeq \frac{1}{\Delta_i} \xi^{m,n}_{\Delta_i}\big(\Delta_i\, h'(h^{-1}(u_i))\,(x_j - h^{-1}(u_i)\big) \\ &\simeq \frac{1}{\Delta_i} \xi^{m,n}_{\Delta_i}(x_j - h^{-1}(u_i)) = \frac{1}{\Delta_i} F_{i,j}. \end{aligned} \tag{52}$$

*In this case, the projection and backprojection step would share the same interpolation model. The sampling steps may be close but are different since they cannot be defined at the same locations (i.e., there exists no bijection between the set of locations $(x_j)_{j \in J}$ and the set of locations $(u_i)_{i \in I}$).*

*ii) For the projection step, the sampling steps $(\Delta_i)_{i \in I}$ are the derivative of $h^{-1}$ at the sampling points $(u_i)_{i \in I}$. When $n = m = 0$, piecewise constant approximations are performed for each signal which matches the description made by geometric models that compute the footprints between pixel and detector bins based on the locations of their edges. It is straightforward to compute sampling steps $\delta_i$ from these edge locations. We define the set of segments of center $h^{-1}(u_i)$ and width $\delta_i$ by setting*

$$\delta_1 = \delta_2 = h^{-1}(u_2) - h^{-1}(u_1) \tag{53}$$

*and, for every $i \in \{2, \ldots, N_I - 1\}$,*

$$h^{-1}(u_{i+1}) - h^{-1}(u_i) = \frac{\delta_{i+1} + \delta_i}{2}. \tag{54}$$

*In this way, given that $(h^{-1}(u_{i+1}) - h^{-1}(u_i))_{1 \leq i \leq N_I - 1}$ is a sequence of increasing steps, the interval $[h^{-1}(u_1), h^{-1}(u_{N_I})]$ is partitioned in intervals $[h^{-1}(u_1), h^{-1}(u_1) + \delta_1/2]$, $(]h^{-1}(u_i) - \delta_i/2, h^{-1}(u_i) + \delta_i/2])_{2 \leq i \leq N_I - 1}$, and $]h^{-1}(u_{N_I}) - \delta_I/2, h^{-1}(u_{N_I})]$. By construction when $l > i$*

$$\frac{h^{-1}(u_l) - h^{-1}(u_i)}{\delta_l} = \frac{1 + \delta_i/\delta_l}{2} + \frac{\sum_{k=i+1}^{l-1} \delta_k}{\delta_l} \geq \frac{1}{2}(1 + \frac{\delta_i}{\delta_l}) \geq \frac{1}{2}. \tag{55}$$

*When $\delta_i$ is substituted for $\Delta_i$ in (24), it follows from Remark 1, that $\mathbf{G} = \mathrm{Diag}(\mathbf{\Delta})$, $\tilde{\mathbf{\Lambda}} = b^n(0)\mathbf{Id}_{N_I}$, where $\mathbf{Id}_{N_I}$ denotes the identity matrix of size $N_I \times N_{I_1}$ and (33) leads to*

$$\mathbf{p} = b^n(0)\mathbf{F}\mathbf{c}. \tag{56}$$

*This provides an alternative way of setting the magnification factors.*

### II.B.4. Low order B-splines characteristics

In our context, low order splines corresponding to $(n, m) \in \{0, 1\}^2$ and $s = m + n + 1 \in \{1, 2, 3\}$ are used. Order 0 indeed provides a good model of the sampling process performed at the physical detector level, while order 1 corresponds to the most common linear interpolation used in signal/image processing. In the following, we give the expression of the quantities which are involved in the proposed spline interpolation procedure. First, we recall the formula of the B-splines of order 0 and 1:

$$(\forall \tau \in \mathbb{R}) \quad \beta^0(\tau) = \begin{cases} 1 & \text{if } |\tau| < \frac{1}{2} \\ 0 & \text{otherwise,} \end{cases}, \qquad \beta^1(\tau) = \begin{cases} 1 - |\tau| & \text{if } |\tau| < 1 \\ 0 & \text{otherwise.} \end{cases} \tag{57}$$

In the implementation, the three main practical aspects are the explicit evaluation of the sampling kernel $\xi_\Delta^{m,n}$, and the multiplication by the inverse of the Gram matrix (i.e., $\tilde{\mathbf{G}}$ for projection). No prefiltering is needed to compute the B-spline coefficients which are equal to the pixel values.

We derive from (22) explicit formulas for correlation functions $\xi_\Delta^{0,0}$, $\xi_\Delta^{1,0}$ ($\xi_\Delta^{0,1}$ being deduced by using (49)), and $\xi_\Delta^{1,1}$:

- **Case 1**

  $$(\forall \theta \in \mathbb{R}) \quad \xi_\Delta^{0,0}(\theta) = \begin{cases} \min(1, \Delta) & \text{if} \quad |\theta| < a_1 \\ a_2 - |\theta| & \text{if} \quad a_1 \le |\theta| < a_2 \\ 0 & \text{if} \quad |\theta| \ge a_2 \end{cases} \tag{58}$$

  with $a_1 = \frac{|\Delta - 1|}{2}$, and $a_2 = \frac{\Delta + 1}{2}$.

- **Case 2**

  $$(\forall \theta \in \mathbb{R}) \quad \xi_\Delta^{1,0}(\theta) = \begin{cases} c_{k,0} + c_{k,1}|\theta| + c_{k,2}|\theta|^2 & \text{for } |\theta| \in [a_{k-1}, a_k[ \\ & \text{and } k \in \{1, 2\} \\ 0 & \text{otherwise} \end{cases} \tag{59}$$

  with $a_0 = 0$, $a_1 = |\frac{\Delta}{2} - 1|$, $a_2 = \frac{\Delta}{2} + 1$, and expressions for $(c_{k,0}, c_{k,1}, c_{k,2})$ given in Table 1. Calculation details can be found in the Appendix.

| **Interval** | $c_{k,0}$ | $c_{k,1}$ | $c_{k,2}$ |
|---|---|---|---|
| $\lvert\theta\rvert < a_1$ | | | |
| if $\Delta \leq 2$ and $\lvert\theta\rvert < \Delta/2$ | $\Delta - \Delta^2/4$ | $0$ | $-1$ |
| if $\Delta \leq 2$ and $\lvert\theta\rvert \geq \Delta/2$ | $\Delta$ | $-\Delta$ | $0$ |
| if $\Delta > 2$ | $1$ | $0$ | $0$ |
| $a_1 \leq \lvert\theta\rvert < a_2$ | | | |
| if $\lvert\theta\rvert \geq \Delta/2$ | $(\Delta^2 + 4\Delta + 4)/8$ | $-1 - \Delta/2$ | $1/2$ |
| if $\lvert\theta\rvert < \Delta/2$ | $(-\Delta^2 + 4\Delta + 4)/8$ | $-1 + \Delta/2$ | $-1/2$ |

Table 1: B-spline correlation function parameters for case 2

- **Case 3** The expression of $\xi_\Delta^{1,1}(\theta)$ is given in Table II. in[15].

Figure 5 displays the 1D kernels. Their width increases with both $\Delta$ and the approximation order. By design, our method makes use of all sampling points therefore the computation cost is proportional to the total number of samples $N_I + N_J$. On the contrary, destination-driven interpolation skips samples when $\Delta > 1$. Thanks to the property (49) of $\xi_\Delta^{m,n}$, the footprints can always be computed using $\Delta < 1$ so that the computation complexity only depends on the order of the splines. The weighted sums will require between two samples for $s = 1$ and four samples when $s = 3$. The computation of $\xi_\Delta^{1,1}$ is complex with several tests to handle. Efficiency relies on using pre-computed look-up tables, with a trade-off between the sizes of the tables and the desired numerical precision.

Finally, when numerical simplifications presented in Remark 2 are implemented, multiplication by $\mathbf{\Lambda}$ and by $\tilde{\mathbf{G}}^{-1}$ reduces to applying the identity except when $n = 1$ where $\tilde{\mathbf{G}}^{-1}$ is the direct cubic filter $(b^3)^{-1}$. Its complexity is proportional to the number of output samples $N_J$, hence it is faster at downsampling. This filter is classically applied according to[20,23] but one can resort to more efficient implementations, for instance on GPU[26] or using FIR filters[27,28].

### II.B.5. Resampling with a 2D representation

Given that axis $v$ is aligned with axis $z$, any cut $f(x, y_0, z)$ of the volume along the plane $y = y_0$ and its projection $p(u, v)$ are related by the homography matrix $\mathbf{H}_{y_0}$ with form (5) satisfying Property (6) i.e., with two null elements, inducing that $u$ does not depend on

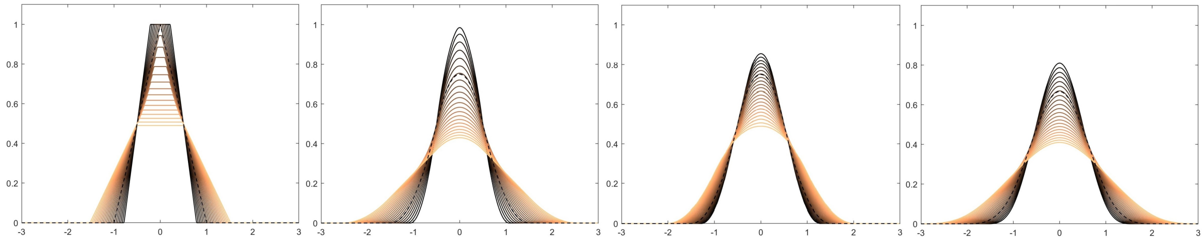

Figure 5: Normalized spline correlation kernels when $\Delta \in [0.5, 2]$. From left to right: $\frac{1}{\Delta}\xi_\Delta^{0,0}$, $\frac{1}{\Delta}\xi_\Delta^{0,1}$, $\frac{1}{\Delta}\xi_\Delta^{1,0}$, $\frac{1}{\Delta}\xi_\Delta^{1,1}$. For $\Delta = 1$, the kernels reduce to B-splines of order 2 (second and third), B-splines of order 1 (first) and B-splines of order 3 (fourth) plotted in dashed lines.

$z$. The presented optimal resampling for 1D magnifications and homographies is sufficient to perform the resampling associated to $\mathbf{H}_{y_0}$. We now investigate the potential of a 2D approach of the problem. We require the following conservation of 2D integrals:

$$\int_{\mathcal{U}\times\mathcal{V}} p(u,v)dudv = \int_{\mathcal{X}\times\mathcal{Z}} f(x,z)dxdz, \tag{60}$$

where $\mathcal{U}\times\mathcal{V}$ and $\mathcal{X}\times\mathcal{Z}$ are suitable domains of integration. It follows from (6) that

$$(\forall (u,v) \in \mathcal{U}\times\mathcal{V}) \quad p(u,v) = f\big(h_1^{-1}(u), h_2^{-1}(u,v)\big)|\det \mathbf{J}_{\mathbf{H}_{y_0}^{-1}}(u,v)|, \tag{61}$$

and the Jacobian $\mathbf{J}_{\mathbf{H}_{y_0}^{-1}}(u,v)$ is given by

$$\mathbf{J}_{\mathbf{H}_{y_0}^{-1}}(u,v) = \begin{pmatrix} \frac{\partial h_1^{-1}(u)}{\partial u} & 0 \\ \frac{\partial h_2^{-1}(u,v)}{\partial u} & \frac{\partial h_2^{-1}(u,v)}{\partial v} \end{pmatrix}, \tag{62}$$

so that $|\det \mathbf{J}_{\mathbf{H}_{y_0}^{-1}}(u,v)| = |\frac{\partial h_1^{-1}(u)}{\partial u}\frac{\partial h_2^{-1}(u,v)}{\partial v}|$.

We now assume that $p$ and $f$ can be decomposed in 2D. Let $N_{I_1}$ and $N_{I_2}$ (resp. $N_{J_1}$ and $N_{J_2}$) be the number of samples along $u$ and $v$ (resp. $x$ and $z$) and let $I_1 = \{1, \dots, N_{I_1}\}$, $I_2 = \{1, \dots, N_{I_2}\}$ (resp. $J_1 = \{1, \dots, N_{J_1}\}$, $J_2 = \{1, \dots, N_{J_2}\}$) be the associated set of indices leading to sets of coordinates $(x_{j_1}, z_{j_2})_{j_1\in J_1, j_2\in J_2}$ and $(u_{i_1}, v_{i_2})_{i_1\in I_1, i_2\in I_2}$. For the projection task, $f$ is decomposed as follows:

$$f(x,z) = \sum_{j_2\in J_2}\sum_{j_1\in J_1} c(j_1,j_2)\,\beta^m(x - x_{j_1})\beta^m(z - z_{j_2}). \tag{63}$$

The two-dimensional representation $p_{\mathbf{\Delta}}$ of the resampling of $p$ is defined by

$$p_{\mathbf{\Delta}}(x,z) = \sum_{i_1\in I_1}\sum_{i_2\in I_2} s_{\mathbf{\Delta}}(i_1,i_2)\,\beta^n_{\Delta_{1,i_1}}(x - h_1^{-1}(u_{i_1}))\beta^n_{\Delta_{2,i_1}}(z - h_2^{-1}(u_{i_1}, v_{i_2})) \tag{64}$$

where $\mathbf{\Delta} = (\Delta_{1,i_1}\Delta_{2,i_1})_{i_1\in I_1}$ is the vector whose components are the products of the diagonal elements of the Jacobian matrix which describes the continuous change of sample rate in $x$

(resp. $z$) along $u$ (resp. $v$), i.e. $\Delta_{1,i_1} = |{h_1^{-1}}'(u_{i_1})|$ and $\Delta_{2,i_1} = \frac{\partial h_2^{-1}(u_{i_1},v_{i_2})}{\partial v}$. We thus use the same values that would appear with successive 1D processing, while verifying

$$p(u_{i_1}, v_{i_2}) = |\det \mathbf{J}_{\mathbf{H}_{y0}^{-1}}(u_{i_1}, v_{i_2})| p_{\boldsymbol{\Delta}}(h_1^{-1}(u_{i_1}), h_2^{-1}(u_{i_1}, v_{i_2})). \tag{65}$$

Let us define the vector $\mathbf{c} = (c(j_1, j_2))_{j_1 \in J_1, j_2 \in J_2}$ (resp. $\mathbf{s}_{\boldsymbol{\Delta}} = (s_{\boldsymbol{\Delta}}(i_1, i_2))_{i_1 \in I_1, i_2 \in I_2}$) whose components have been indexed according to $(j_1 - 1)N_{J_2} + j_2$ (resp. $(i_1 - 1)N_{I_1} + i_2$).
The normal equations in 2D are expressed in matrix form as

$$\mathbf{G}\mathbf{s}_{\boldsymbol{\Delta}} = \mathbf{F}\mathbf{c}, \tag{66}$$

where $\mathbf{F} \in [0, +\infty[^{N_{I_1} N_{I_2} \times N_{J_1} N_{J_2}}$ and $\mathbf{G} \in [0, +\infty[^{N_{I_1} N_{I_2} \times N_{I_1} N_{I_2}}$ are such that, for every $i = (i_1 - 1)N_{I_2} + i_2$, $j = (j_1 - 1)N_{J_2} + j_2$ and $l = (l_1 - 1)N_{I_2} + l_2$ with $(i_1, l_1) \in I_1^2$, $(i_2, l_2) \in I_2^2$, $j_1 \in J_1$, and $j_2 \in J_2$,

$$\begin{aligned} F_{i,j} &= \int_{-\infty}^{+\infty} \int_{-\infty}^{+\infty} \beta^m(x - x_{j_1}) \beta^n_{\Delta_{1,i_1}}(x - h_1^{-1}(u_{i_1})) \beta^m(z - z_{j_2}) \beta^n_{\Delta_{2,i_1}}(z - h_2^{-1}(u_{i_1}, v_{i_2})) dx dz \\ &= \xi^{m,n}_{\Delta_{1,i_1}}(x_{j_1} - h_1^{-1}(u_{i_1})) \xi^{m,n}_{\Delta_{2,i_1}}(z_{j_2} - h_2^{-1}(u_{i_1}, v_{i_2})) \end{aligned} \tag{67}$$

and

$$\begin{aligned} G_{j,l} &= \left(\beta^n_{\Delta_{2,l_1}} * \beta^n_{\Delta_{2,i_1}}(h_2(u_{i_1}, v_{i_2}) - h_2(u_{l_1}, v_{l_2}))\right) \left(\beta^n_{\Delta_{1,l_1}} * \beta^n_{\Delta_{1,i_1}}(h_1^{-1}(u_{i_1}) - h_1^{-1}(u_{l_1}))\right) \\ &= \Delta_{2,i_1} \Delta_{1,i_1} \xi^{n,n}_{\Delta_{2,l_1}/\Delta_{2,i_1}} \left(\frac{h_2^{-1}(u_{i_1}, v_{i_2}) - h_2^{-1}(u_{l_1}, v_{l_2})}{\Delta_{2,j_1}}\right) \xi^{n,n}_{\Delta_{1,l_1}/\Delta_{1,i_1}} \left(\frac{h_1^{-1}(u_{i_1}) - h_1^{-1}(u_{l_1})}{\Delta_{1,i_1}}\right). \end{aligned} \tag{68}$$

Since $h_1^{-1}$ does not depend on $v$, separability of $\mathbf{F}$ is achieved as

$$\mathbf{F} = \begin{bmatrix} (F_1)_{1,1} \mathbf{F}_2^1 & \dots & (F_1)_{N_{I_1},1} \mathbf{F}_2^{N_{I_1}} \\ \vdots & \dots & \vdots \\ (F_1)_{1,N_{J_1}} \mathbf{F}_2^1 & \dots & (F_1)_{N_{I_1},N_{J_1}} \mathbf{F}_2^{N_{I_1}} \end{bmatrix} = \left[(\mathbf{F}_1)_{1,*} \otimes \mathbf{F}_2^1 \quad \dots \quad (\mathbf{F}_1)_{N_{I_1},*} \otimes \mathbf{F}_2^{N_{I_1}}\right], \tag{69}$$

where ⊗ denotes the Kronecker product. Matrix $\mathbf{F}_1 \in [0, +\infty[^{N_{I_1} \times N_{J_1}}$ is such that, for every $i_1 \in I_1$ and $j_1 \in J_1$,

$$(F_1)_{i_1,j_1} = \xi^{m,n}_{\Delta_{1,i_1}}(x_{j_1} - h_1^{-1}(u_{i_1})). \tag{70}$$

For every $i_1 \in I_1$, $(\mathbf{F}_1)_{i_1,*}$ denotes the $i_1$-th row of $\mathbf{F}_1$ and matrix $\mathbf{F}_2^{i_1} \in [0, +\infty[^{N_{I_2} \times N_{J_2}}$ is such that, for every $i_2 \in I_2$ and $j_2 \in J_2$,

$$({F_2}^{i_1})_{i_2,j_2} = \xi^{m,n}_{\Delta_{2,i_1}}(z_{j_2} - h_2^{-1}(u_{i_1}, v_{i_2})). \tag{71}$$

Then, vector $\mathbf{p} = (p(u_{i_1}, v_{i_2}))_{i_1 \in I_1, i_2 \in I_2} \in \mathbb{R}^{N_{I_1} N_{I_2}}$ (whose components are indexed according to $(i_1 - 1)N_{I_2} + i_2$) is expressed as

$$\mathbf{p} = (\mathrm{Diag}(\boldsymbol{\Delta}) \otimes \mathbf{Id}_{N_{I_2}})\tilde{\boldsymbol{\Lambda}}\mathbf{G}^{-1}\mathbf{F}\mathbf{c}, \tag{72}$$

where matrix $\tilde{\boldsymbol{\Lambda}} \in [0, +\infty[^{N_{I_1}N_{I_2} \times N_{I_1}N_{I_2}}$ is such that, for every $i = (i_1 - 1)N_{I_2} + i_2$ and $l = (l_1 - 1)N_{I_2} + l_2$, with $(i_1, l_1) \in I_1^2$, $(i_2, l_2) \in I_2^2$,

$$\tilde{\Lambda}_{i,l} = \beta^n_{\Delta_{1,l_1}} \left(h_1^{-1}(u_{i_1}) - h_1^{-1}(u_{l_1})\right) \beta^n_{\Delta_{2,l_1}} \left(h_2^{-1}(u_{i_1}, v_{i_2}) - h_2^{-1}(u_{l_1}, v_{l_2})\right). \tag{73}$$

Since we use the same low order B-splines, for every $(i_1, l_1) \in I_1^2$ for which

$$|h_1^{-1}(u_{i_1}) - h_1^{-1}(u_{l_1})| \leq (n+1)\frac{\Delta_{1,i_1} + \Delta_{1,l_1}}{2}, \tag{74}$$

we can again assume that $u_{i_1}$ and $u_{l_1}$ are close enough so that $\frac{\partial h_2^{-1}}{\partial v}(u_{i_1}, v_{i_2}) \simeq \frac{\partial h_2^{-1}}{\partial v}(u_{l_1}, v_{l_2})$, leading to

$$\Delta_{2,i_1} \xi^{n,n}_{\Delta_{2,l_1}/\Delta_{2,i_1}} \left(\frac{h_2^{-1}(u_{i_1}, v_{i_2}) - h_2^{-1}(u_{l_1}, v_{l_2})}{\Delta_{2,i_1}}\right) \simeq \sqrt{\Delta_{2,i_1}\Delta_{2,l_1}}\beta^{2n+1}\left(v_{i_2} - v_{l_2}\right). \tag{75}$$

In matrix form, this translates to the following approximation:

$$\mathbf{G} \simeq \mathbf{G}_1 \otimes \tilde{\mathbf{G}}_2, \tag{76}$$

where the elements of $\mathbf{G}_1 \in [0, +\infty[^{N_{I_1} \times N_{I_1}}$ and $\tilde{\mathbf{G}}_2 \in [0, +\infty[^{N_{I_2} \times N_{I_2}}$ are, for every $(i_1, l_1) \in I_1^2$,

$$(G_1)_{i_1,l_1} = \Delta_{1,i_1}\sqrt{\Delta_{2,i_1}\Delta_{2,l_1}}\xi^{n,n}_{\Delta_{1,l_1}/\Delta_{1,i_1}} \left(\frac{h_1^{-1}(u_{i_1}) - h_1^{-1}(u_{l_1})}{\Delta_{1,i_1}}\right) \tag{77}$$

and, for every $(i_2, l_2) \in I_2^2$,

$$(\tilde{G}_2)_{i_2,l_2} = \beta^{2n+1}\left(v_{i_2} - v_{l_2}\right). \tag{78}$$

It can be noticed that both $\mathbf{G}_1$ and $\tilde{\mathbf{G}}_2$ are symmetric matrices. Likewise $\tilde{\boldsymbol{\Lambda}}$ can be approximated as

$$\tilde{\boldsymbol{\Lambda}} \simeq \tilde{\boldsymbol{\Lambda}}_1 \otimes \boldsymbol{\Lambda}_2, \tag{79}$$

where the elements of $\tilde{\boldsymbol{\Lambda}}_1 \in [0, +\infty[^{N_{I_1} \times N_{I_1}}$, $\boldsymbol{\Lambda}_2 \in [0, +\infty[^{N_{I_2} \times N_{I_2}}$ are, for every $(i_1, l_1) \in I_1^2$ and $(i_2, l_2) \in I_2^2$,

$$(\tilde{\Lambda}_1)_{i_1,l_1} = \beta^n_{\Delta_{1,l_1}}\left(h_1^{-1}(u_{i_1}) - h_1^{-1}(u_{l_1})\right), \quad (\Lambda_2)_{i_2,l_2} = \beta^n_1(v_{i_2} - v_{l_2}). \tag{80}$$

Finally, $\mathbf{p}$ can be derived as

$$\begin{aligned}\mathbf{p} &\simeq (\mathrm{Diag}(\boldsymbol{\Delta}) \otimes \mathbf{Id}_{N_{I_2}})(\tilde{\boldsymbol{\Lambda}}_1 \otimes \boldsymbol{\Lambda}_2)(\mathbf{G}_1^{-1} \otimes \tilde{\mathbf{G}}_2^{-1})\mathbf{Fc} \\ &= \big((\mathrm{Diag}(\boldsymbol{\Delta})\tilde{\boldsymbol{\Lambda}}_1\mathbf{G}_1^{-1}) \otimes (\boldsymbol{\Lambda}_2\tilde{\mathbf{G}}_2^{-1})\big)\mathbf{Fc}. \end{aligned} \tag{81}$$

As long as the magnification of the B-splines provides a good enough approximation of the change of sampling rates induced by the homography, the 2D solution is separable into 1D computations. Note that (81) shares the same footprint as would be obtained by applying our 1D resampling approach separately on each row and column.

The backprojection task uses the reverse geometric transforms

$$\begin{cases} u = h_1(x) \\ v = h_2(x, z). \end{cases} \tag{82}$$

The magnification factors are then chosen equal to $\Delta'_{1,j_1} = |h'_1(x_{j_1})|$ and $\Delta'_{2,j_1} = \frac{\partial h_2(x_{j_1}, z_{j_2})}{\partial z} = h_{22}/s(x_{j_1})$ where $j_1 \in J_1$ and $j_2 \in J_2$. Hereafter, we will denote $\mathbf{H}_s$ the discretized homographic transform involved in backprojection implemented as (81) and $\tilde{\mathbf{H}}_s^{-1}$ the discretized homographic transform involved in projection for $s = m + n + 1$. Let $L$ be the number of voxels in the volume and $K$ be the number of detector cell measurements acquired in a conic geometry with a flat panel detector. Applying this pipeline to all homographies $\mathbf{H}_s$ and $\tilde{\mathbf{H}}_s^{-1}$ deduced from projection matrix $\mathbf{P}$ gives rise to backprojection matrix $\mathbf{B}_s \in \mathbb{R}^{L \times K}$ for analytic reconstruction and forward projection matrix $\mathbf{R}_s$ for MBIR.

## II.C. Special cases

Within our formalism, several conventional projection models can be revisited and their limitations highlighted.

### II.C.1. Destination-driven interpolation

Destination-driven backprojection with homography matrices $\mathbf{H}$ is straightforward: from arbitrary "destination" location $(x_{j_1}, z_{j_2})$, the corresponding coordinates onto the detector $(u, v)$ are computed according to (5). Then interpolation takes place in the projection space. Likewise, destination-driven forward projection based on $\mathbf{H}^{-1}$ is straightforward: it steps through destination locations i.e. every bin center $(u_{i_1}, v_{i_2})$ and finds the corresponding set of voxels in the volume that map into the output. Setting $(u_{i_1}, v_{i_2})$ into (5) yields the equation of the line that goes from location $(u_{i_1}, v_{i_2})$ to the focal point $S$. Numerical integration of volume $f$ is then performed over this line (or ray) by means of interpolation in the volume space. The most common instance of this approach consists in using bilinear interpolation. For 1D projection, this amounts to plugging $h^{-1}(u_i)$ in (23) with $m = 1$. Our framework offers an alternative interpretation of this approach. In (33) if we set $n = m = 0$ and define set $\mathbf{\Delta}$ with constant sampling step 1 in the normal equations (27), then the destination-driven projection footprint matrix $\mathbf{F}$ is such that, for every $i \in I$ and $j \in J$,

$$F_{i,j} = \xi_1^{0,0}(x_j - h^{-1}(u_i)) = \beta^1(x_j - h^{-1}(u_i)) \tag{83}$$

while the destination-driven backprojection footprint matrix $\mathbf{F}'$ in (37) is

$$F'_{j,i} = \xi_1^{0,0}(u_i - h(x_j)) = \beta^1(u_i - h(x_j)). \tag{84}$$

Even though both $\mathbf{F}$ and $\mathbf{F}'$ use $\beta^1$, they rely on different representations so that they are far from being the transpose of each other. This teases out the "magnification-agnostic" nature of such projection and backprojection models, thus explaining their limitations in terms of adjoint and noise handling as we will show further on in our numerical experiments.

### II.C.2. Distance-driven interpolation

The DD model has been proposed as an alternative to bilinear interpolation. Similar to our approach, the model captures both sides of the sampling process, at the voxel and detector bin levels, but from the perspective of a geometrical discretization, which is not specific to flat panel detector and therefore not relying on projection matrices and homographies. For planar parallel or fan-beam geometry, or when separability holds, the 1D version is used as follows: voxels and bins are located by their edges on their respective axis. These locations are mapped according to the system geometry onto a common axis. Interpolation between one voxel and one bin is computed as the length of the overlapping segment footprints of the voxel and the bin over this axis as shown in Figure 2 of[9]. Under this choice, the scheme is neither destination nor source driven, rendering it equally adequate for projection and backprojection. This results in a matched pair (up to normalization factors) for this particular axis.

Remarkably, for projection, for every $i \in I$ and $j \in J$,

$$\xi^{0,0}_{\Delta_i}(h^{-1}(u_i) - x_j) = \int_{-\infty}^{+\infty} \beta^0_1(\tau)\beta^0_{\Delta_i}(h^{-1}(u_i) - x_j - \tau)d\tau = \int_{x_j-\frac{1}{2}}^{x_j+\frac{1}{2}} \beta^0_{\Delta_i}(h^{-1}(u_i) - \tau)d\tau. \tag{85}$$

The above integral is equal to the intersection of the support of $\beta^0_1$ centered at $x_j$ and of length 1, with that of $\beta^0_{\Delta_i}$ centered at $h^{-1}(u_i)$ and of length $\Delta_i$, which is the quantity at the core of the DD scheme. Function $\beta^0_{\Delta_i}(h^{-1}(u_i) - \cdot)$ can be viewed as the projection of the detector bin centered at $u_i$, that is a segment centered at $h^{-1}(u_i)$ with length $\Delta_i$. As a result, in the context of flat panel cone beam geometry, the DD scheme can be expressed in our framework with $n = m = 0$ with a slightly different set of magnification factors $\boldsymbol{\Delta}^{\mathrm{DD}}$ as described in Remark 3ii. In particular, our choice of setting $\boldsymbol{\Delta}^{\mathrm{DD}} = \boldsymbol{\Delta}'$ corresponds to the case when the intermediary axis is chosen as the detector axis, while setting $\boldsymbol{\Delta}^{\mathrm{DD}} = \boldsymbol{\Delta}$ corresponds to magnifications at the voxel axis. In the following, we shall not discuss this degree of freedom of the method, we will instead consider the DD with any intermediate axis and associated set of magnifications as being an instance of our approach when $n = m = 0$.

## II.D. Data rebinning and rectification

If one were allowed infinite computing resources, with a potentially considerable amount of oversampling, any interpolation scheme would be equally satisfying. But the clinical constraints of fast reconstruction, simple workflow, and limited storage capability require downsampling, which induces a loss of information and forces optimizing image and data representations, even for analytical reconstruction. In current medical practice, the reconstructed slices are of size $512 \times 512$ while X-ray flat panels with pitch of $200\mu$ can deliver many more samples, yielding a small ratio $\alpha/t_z$ in (2) and (3), i.e. a large downsampling.
In that case, destination-driven backprojection will miss samples and will not make use of the full X-ray dose. To circumvent this issue, a prior rebinning of the data to larger pixels trades resolution loss for noise and aliasing reduction. The term "rebinning" refers to using constant magnifications of integer factors at the detector level. Our model embeds the magnifications factors, hence alleviating the need for rebinning. Another resampling transform that may be used for reconstruction is "rectification"[24]. Rectification relies on the observation that, for any paired homographies $(\mathbf{H}_{y_0}, \mathbf{H}_{y_1})$ derived from projection matrix $\mathbf{P}$, each one can be deduced from the other by a magnification. The decomposition of the projection

into a composition of homographies can thus be simplified into computing a single "rectification" homography derived from, e.g. $\mathbf{H}_{y_0}$, to which 2D magnification $\mathbf{H}_{y_1}\mathbf{H}_{y_0}^{-1}$ is applied to obtain $\mathbf{H}_{y_1}$. As magnifications present a better computation layout than homographies, rectification has been introduced to get faster projector-backprojector pairs for both FBP and MBIR. Resampling based on the convolution of B-splines is an obvious candidate for both steps. A model of order $n = 0$ for the detector data perfectly matches the acquisition process, that is an integration over a surface. In contrast, the resampled signal at an optimized sampling step $\Delta$ or through rectification becomes the data of a virtual detector that may be described by a higher order basis function.

In the case of MBIR, the ratio of $K$, the number of known values, over $L$, the number of unknowns, strongly influences the conditioning of matrix $\mathbf{R}_s$. Using smaller voxels increases $L$ and degrades the conditioning of $\mathbf{R}_s$ because the angular sampling becomes insufficient. Since it is not possible to oversample the data in the angular direction, downsampling of the data is again part of the problem. One important advantage of MBIR is to allow for accurate noise modeling in the observation model. Noise models are simple and accurate, when directly modeling the detector statistically-independent bin measurements. To preserve the noise model and comply with computation constraints, rebinning by block-averaging is sometimes used. Resizing with a non-necessarily integer factor is less restrictive, but bilinear interpolation modifies the noise properties by introducing correlations. One expected outcome of using convolutions of B-splines is to provide less alteration of the noise properties to allow one to keep a simple noise model after data resampling, whether after a magnification by a real factor or a rectification homography. Together with a better noise handling, MBIR allows for improved resolution. Note again that a B-spline of order 0 at the detector level is a faithful resolution degradation model, but a large cubic voxel model may not be appropriate for representing a higher resolution volume. Our approach shows how to introduce a higher level of precision for the solution.

Another benefit of MBIR is to reduce the undersampling artifacts appearing for instance in CBCT with a circular orbit or with a limited number of projections[2]. Missing projections is obviously independent of the interpolation scheme within a projection; in that case an accurate model is one that minimizes interpolation errors[17]. This is easier to achieve using a virtual rectified detector with 2D magnifications where the order of the B-spline sets the compromise between speed and precision.

We see that there is no one-fit-for-all discretization, but B-splines adapt remarkably well to one's various needs.

### II.D.1. Rotated cone-beam geometry

Up to now, the cone-beam geometry has been assumed to have axis $v$ aligned with axis $z$. When a 2D rotation within the detector plane can make the axes parallel again, it can be computed within the same framework of centered B-splines and separable 1D processing[25] and can be merged with the steps of rebinning or rectification.

Otherwise, in the practical case of the vibrations of a C-arm system, the rotations that break the parallelism at each angle are small. They cannot be ignored without degrading the resolution, but they can be neglected in the definition of the set of magnifications. We therefore now assume that the null elements, $h_{3,2}$ and $h_{1,2}$ of $\mathbf{H}_{y_0}$ in (5) are replaced by small nonzero values. In this case $\frac{\partial h_1^{-1}}{\partial v}$ no longer vanishes. We use the diagonal elements of the Jacobian, considered as a sufficient description of the local magnifications, while keeping the correct projection matrix to compute the sampling points locations. This yields magnification factors $(\Delta_{1,i_1,i_2}, \Delta_{2,i_1,i_2})_{i_1 \in I_1, i_2 \in I_2}$. In this case, the elements of $\mathbf{F}$ are

$$F_{i,j} = \xi^{m,n}_{\Delta_{1,i_1,i_2}}(x_{j_1} - h_1^{-1}(u_{i_1}, v_{i_2}))\xi^{m,n}_{\Delta_{2,i_1,i_2}}(z_{j_2} - h_2^{-1}(u_{i_1}, v_{i_2})) \tag{86}$$

and $(\mathrm{Diag}(\boldsymbol{\Delta}) \otimes \mathbf{Id}_{N_{I_2}})$ has to be replaced by the diagonal matrix whose $i$-th diagonal elements for $i = (i_1 - 1)N_{I_2} + i_2$ with $i_1 \in I_1$ and $i_2 \in I_2$ is equal to $|\det \mathbf{J}_{\mathbf{H}_{y_0}^{-1}}(u_{i_1}, v_{i_2})|$. Note that separability of $\mathbf{F}$ and the scaling diagonal matrix no longer holds. We can neglect $h_{3,2}$ for matrices $\mathbf{G}$ and $\tilde{\boldsymbol{\Lambda}}$ to resort to the same surrogate matrices as in the ideal case. Assuming small rotations, the gradient $\frac{\partial h_1^{-1}}{\partial v}$ is small and using such model is expected to outperform linear interpolation that ignores magnifications.

## III. Experiments

We tested our magnification-driven interpolation scheme for cone-beam projection using orders $(n, m) \in \{0, 1\}^2$ with $m \geq n$. The discrete forward projector and the discrete backprojector based on linear interpolation taken as a reference, are denoted by $\mathbf{R}_r$ and $\mathbf{B}_r$. The corresponding homographic transforms are denoted by $\tilde{\mathbf{H}}_r^{-1}$ and $\mathbf{H}_r$. In the previous sections, we proposed various simplified implementations of forward projectors and backprojectors.

Henceforth, we will use a label a, b, or c to specify the chosen implementation. For backprojection, implementation a consists in computing $\mathbf{p}$ according to (81) using inversion of tridiagonal matrices[12,22]. Implementation b consists in substituting $\operatorname{Diag}(\boldsymbol{\Delta})^{-1/2}\mathbf{T}_n^{-1}\operatorname{Diag}(\boldsymbol{\Delta})^{-1/2}$ for $\mathbf{G}_1^{-1}$ in (81). Based on implementation b, implementation c consists in further replacing $\tilde{\boldsymbol{\Lambda}}_1$ by $\boldsymbol{\Lambda}_1$. It can be noticed that, given the range values of $(n, m)$, (81) then becomes

$$\mathbf{p} = \big((\operatorname{Diag}(\boldsymbol{\Delta})^{1/2}\mathbf{T}_n^{-1}\operatorname{Diag}(\boldsymbol{\Delta})^{-1/2}) \otimes \tilde{\mathbf{G}}_2^{-1}\big)\mathbf{F}\mathbf{c}. \tag{87}$$

Note that with c, post-filtering through operator $\tilde{\mathbf{G}}_2^{-1}$ in (87) is completely independent from the homography step. By linearity, it can thus be performed in a single global pass, after summation of each transformed planes, on the resulting projections (or on the volume for backprojection).

## III.A. Simulation scenarios

An ideal cone-beam geometry is considered, made of 600 projections matrices covering a 360° circular acquisition. By ideal, we mean that the trajectory of the source point is strictly planar and that the optical axis always crosses the center of rotation and hits the center of the detector which gives $t_x = t_y = u_0 = v_0 = 0$. All projection matrices are thus of the form

$$\mathbf{P} = \begin{pmatrix} \alpha\cos\theta & \alpha\sin\theta & 0 & 0 \\ 0 & 0 & \alpha & 0 \\ -\sin\theta & \cos\theta & 0 & t_z \end{pmatrix}. \tag{88}$$

The detector size is such that the data is never truncated. Iso-sampling is defined as $t_z = \alpha = 1500$ voxels. The set of magnification factors for approximating the homographies is defined at the destination level, namely at the detector level for $\mathbf{R}_s$ and at the volume level for $\mathbf{B}_s$. Recall that these operators rely on the repeated use of operators $\mathbf{H}_s$ and $\tilde{\mathbf{H}}_s^{-1}$ for various matrices $\mathbf{H}$. We also considered forward and backward projector $\mathbf{V}_s$ corresponding to the discretization of the associated rectified virtual geometry made of magnifications only. The latter case serves as a baseline since it is known that magnification-driven interpolation fulfills optimality conditions for magnifications[15].

## III.B. Tasks

Projection for the whole orbit involves a mix of homographies, from simple magnification when the detector is aligned with the volume to the worst case for a Cartesian grid at $\pi/4$. The impact of such homographies is over coronal and sagittal slices. Therefore, we first tested our different implementations of $\mathbf{H}_s$ and $\tilde{\mathbf{H}}_s^{-1}$ for the matrix $\mathbf{H}$ deduced from $\theta = \pi/4$ and $y = 0$ as

$$\mathbf{H} = \begin{pmatrix} \alpha & \alpha \sin \pi/4 & 0 \\ 0 & \alpha & 0 \\ -\sin \pi/4 & 0 & t_z \end{pmatrix}. \qquad (89)$$

We tested resampling steps $\delta_H = \alpha/t_z \in \{1, 2, 3.5\}$, where $\delta_H = 1$ means isosampling and $\delta_H > 1$ means that the voxel size is chosen $\delta_H$ times bigger than isosampling, that is a downsampling by factor $\delta_H$ is performed.

Projectors and backprojectors themselves were evaluated through tasks of analytical and iterative reconstructions. For analytical reconstruction, each model $\mathbf{R}_r$ and $\mathbf{R}_s$ was successively used to simulate the projection of a vertical edge at isosampling followed by FDK reconstruction with the corresponding operator $\mathbf{B}_r$ or $\mathbf{B}_s$. At backprojection, all projection matrices were rotated by angle atan(1/16) to yield a slanted edge in the reconstructed image so that the edge is sampled with 16 sub-voxel shifts. For iterative reconstruction, the pair $(\mathbf{R}_s, \mathbf{R}_s^\top)$ is employed. For a given forward model $\mathbf{R}_s$, MBIR was the result of minimizing the following objective function:

$$\Psi(\mathbf{f}) = \frac{1}{2}\|\mathbf{R}_s\mathbf{f} - \mathbf{p}\|_2^2 + \frac{\beta}{2}\|\mathbf{f}\|_2^2. \qquad (90)$$

Parameter $\beta$, set to $2 \times 10^{-2}$, ensures the strong convexity of the cost function $\Psi$, and thus the uniqueness of the minimizer. The initial value for volume $\mathbf{f}$ was set to the zero vector. The minimization problem was solved by simple gradient descent. Vector $\mathbf{p}$ is the projection of the $512 \times 512$ image displayed in Figure 6 (right) with $\mathbf{R}_r$ using an 8 times oversampling followed by an $8 \times 8$ bin averaging.

## III.C. Image quality metrics

We compared the models in terms of bias (accounting for the loss of spatial resolution or presence of artifacts) and noise propagation. For visual assessment of bias, we used two

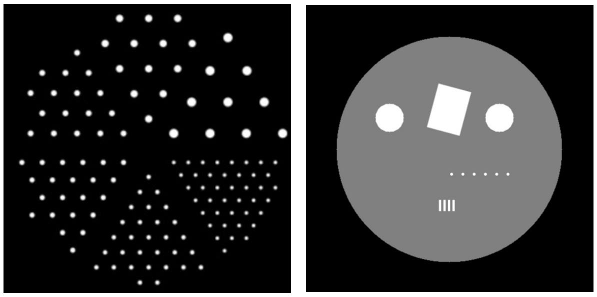
(a) (b)

Figure 6: Reference images. Left: resolution image. Right: phantom for iterative reconstruction (axial slice).

simulated images (Figure 6): a ”wire” image made of cylinders of varying diameters and fixed intensity set to 100, and a phantom containing sharp geometrical shapes (two cylinders, one rectangles, six wires and one line pair pattern). Spatial resolution was assessed by computing the modulation transfer functions (MTF) of the FDK-reconstructed slanted edge. Bias was evaluated for MBIR as the root mean square error (RMSE) with respect to the ground truth over uniform ROIs.

For noise propagation, we used ensemble statistics: for two different operations (homography $\mathbf{H}_s$ and backprojection $\mathbf{B}_s$), $N$ statistical replicates of noise were processed by the same operation so that mean, standard deviation (STD), and signal-to-noise ratio (SNR), taken as the ratio of mean to standard deviation, can be computed at each pixel of the output after processing. The 2D Noise Power Spectrum (NPS) over a circular region-of-interest can also be computed and averaged radially. The noise, added on each operation input, was always independent and identically distributed, zero-mean and Gaussian with variance set to 1 for each test of $\mathbf{H}_s$ and to $10^3$ for tasks involving $\mathbf{B}_s$.

## III.D. C-arm CBCT data

An exemplary real-data case is also studied. A CBCT acquisition of a quality assurance phantom containing a resolution section with bar patterns was obtained on a GE Healthcare C-arm system with a circular orbit of 200° sampled by 607 projections. The detector bin size was 0.2 mm. The distance from the focal spot to the detector is 1295 mm which yields $\alpha = 1295/0.2 = 6475$. The distance from the focal spot to the center of rotation is 820 mm. The voxel size at isosampling is 0.127 mm ($t_z = 820/0.127 = 6456$). A $512 \times 512$ image with this voxel size yields a field of view of 65 mm only. We therefore compared the performance of interpolation for the voxel size at isosampling and for a four times bigger field of view by increasing the voxel size to 0.508 mm. For the latter case, we compared FDK reconstructions with the following three options: i) direct backprojection of the original data ($\alpha = 1295/0.2$, $t_z = 820/0.508$), ii) rectification of the original data ($\alpha = 1295/0.200$, $t_z = 820/0.127$) followed by backprojection in rectified geometry ($\alpha = 820/0.127$, $t_z = 820/0.508$) and iii) bin averaging by a factor 4, designated by operator $\mathbf{A}$, followed by direct backprojection ($\alpha = 1295/0.800$, $t_z = 820/0.508$). We compared the reconstruction of the bar-pattern of 8 line pairs per mm on an axial slice 7.62 mm away from the central slice. This pattern is perfectly resolved by the system when the voxel size is equal to 0.127 mm, but it is degraded for a voxel size of 0.508 mm. The amount of degradation induced by the large voxel size depends on the interpolation only, not on the system. In such real-data conditions, Equation (6) is not rigorously satisfied, hence we fall in the situation described in Section II.D.1..

# IV. Experimental results

## IV.A. Homography

| | $\mathbf{H}_1$ | | $\mathbf{H}_2$ | | $\mathbf{H}_3$ | | $\tilde{\mathbf{H}}_1^{-1}$ | | $\tilde{\mathbf{H}}_2^{-1}$ | | $\tilde{\mathbf{H}}_3^{-1}$ | |
|---|---|---|---|---|---|---|---|---|---|---|---|---|
| | b | c | b | c | b | c | b | c | b | c | b | c |
| $\delta_H = 1$ | 0 | 0 | 5.2 | 22 | 4.6 | 20 | 53 | 53 | 49 | 56 | 46 | 53 |
| $\delta_H = 2$ | 0 | 0 | 37 | 54 | 35 | 52 | 10 | 10 | 27 | 31 | 26 | 30 |
| $\delta_H = 3.5$ | 0.1 | 0.1 | 25 | 25 | 24 | 25 | 1.8 | 1.8 | 0.2 | 2.9 | 0.2 | 2.4 |

Table 2: Comparison of implementations b and c with respect to implementation a in terms of RMSE ($\times 10^{-3}$)

Table 2 reports measures of RMSE associated to implementations b and c with respect to implementation a after applying either homography $\tilde{\mathbf{H}}_s^{-1}$ or $\mathbf{H}_s$ with our splines of order $s = m + n + 1$ on the wire image degraded by noise. First, for all models, the errors are very low. For $\delta_H > 1$, $\mathbf{H}_s$ corresponds to a downsampling while $\tilde{\mathbf{H}}_s^{-1}$ performs an upsampling. We see that almost no error is made when performing a downsampling with our lowest order model. Moreover, implementations b and c are on average 1.15 and 1.4 times faster than implementation a for the considered homographies. Based on these facts, we now focus on implementation c and drop the corresponding index.

Figure 7 (top) shows the wire images obtained after performing a homography with $\delta_H = 3.5$ followed by the inverse homography. One can notice that the image obtained with linear interpolation i.e. $\tilde{\mathbf{H}}_r^{-1}\mathbf{H}_r$ lacks some wires as indicated by the arrow on Figure 7 (bottom left). This highlights the issue of nonstationarity with linear interpolation. With the proposed magnification-driven interpolation, all wires are visible. The images obtained with $\tilde{\mathbf{H}}_1^{-1}\mathbf{H}_1$ have a patchy look typical of 0-order B-spline models. The highest order B-spline model gives the images with the least distortion at the price of small undershoots. These differences between models are less apparent for lower downsampling factors as illustrated for $\delta_H = 1$ by Figure 7 (bottom right) showing the profile through the three bottom right wires (solid box) on the bottom left Figure. The profiles with $\tilde{\mathbf{H}}_2^{-1}\mathbf{H}_2$ and $\tilde{\mathbf{H}}_3^{-1}\mathbf{H}_3$ show higher resolution than $\tilde{\mathbf{H}}_r^{-1}\mathbf{H}_r$ and $\tilde{\mathbf{H}}_1^{-1}\mathbf{H}_1$.

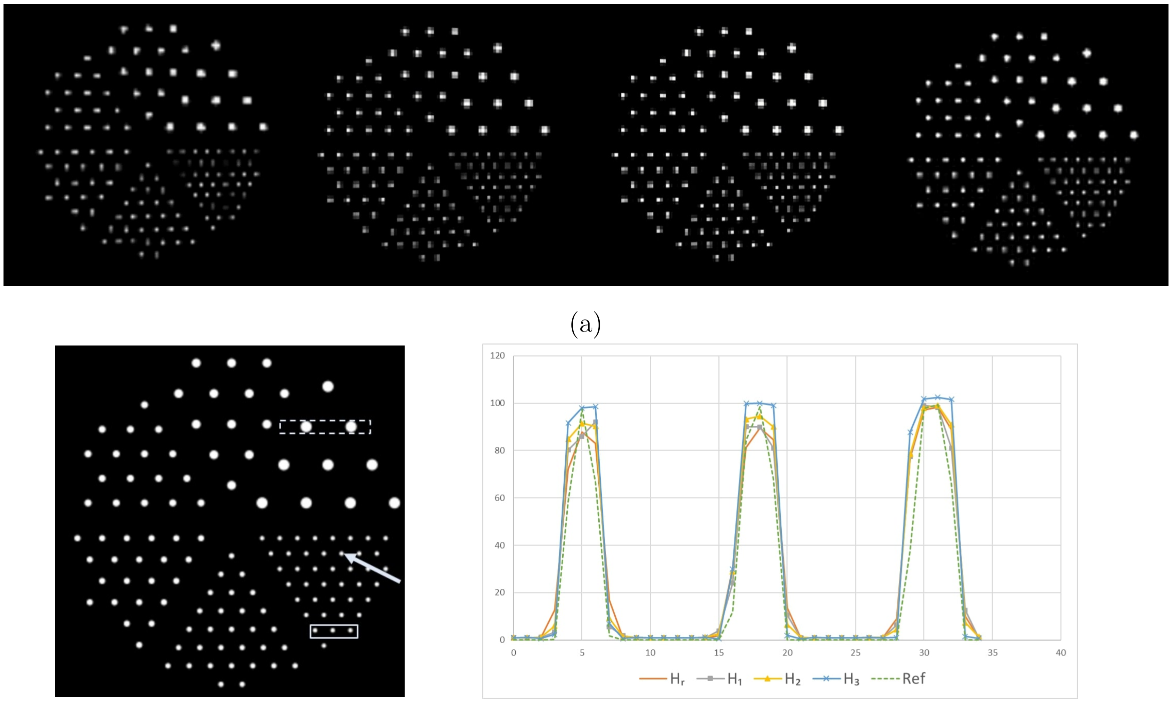

(a)

(b)

(c)

Figure 7: Assessment of resolution for direct and inverse homography. Top: output wire slice using $\delta_H = 3.5$ ; from left to right: $\tilde{\mathbf{H}}_r^{-1}\mathbf{H}_r$, $\tilde{\mathbf{H}}_1^{-1}\mathbf{H}_1$, $\tilde{\mathbf{H}}_2^{-1}\mathbf{H}_2$, $\tilde{\mathbf{H}}_3^{-1}\mathbf{H}_3$. Bottom left: input resolution image. Bottom right: plots through three wires (solid box in the bottom left Figure) using $\delta_H = 1$.

Figure 8 shows the SNR images obtained from $N = 200$ replicate homographies $\tilde{\mathbf{H}}_s^{-1}\mathbf{H}_s$ and $\tilde{\mathbf{H}}_r^{-1}\mathbf{H}_r$ for $\delta_H = 2.025$. The window widths (WW) and window levels (WL) are set independently for each image. We see that noise correlations appear along the columns where the homography is a magnification, while along the rows, the varying local magnification factor

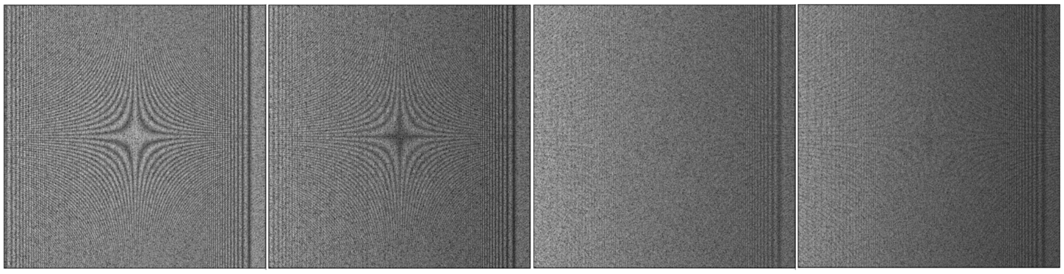

Figure 8: SNR images using $\delta_H = 2$. From left to right: $\tilde{\mathbf{H}}_r^{-1}\mathbf{H}_r$, $\tilde{\mathbf{H}}_1^{-1}\mathbf{H}_1$, $\tilde{\mathbf{H}}_2^{-1}\mathbf{H}_2$, $\tilde{\mathbf{H}}_3^{-1}\mathbf{H}_3$.

| | $\tilde{\mathbf{H}}_r^{-1}\mathbf{H}_r$ | $\tilde{\mathbf{H}}_1^{-1}\mathbf{H}_1$ | $\tilde{\mathbf{H}}_2^{-1}\mathbf{H}_2$ | $\tilde{\mathbf{H}}_3^{-1}\mathbf{H}_3$ |
|---|---|---|---|---|
| $\delta_H = 1$ | $29 \pm 7.8$ | $28 \pm 7.9$ | $25 \pm 4.5$ | $21 \pm 3.7$ |
| $\delta_H = 2$ | $29 \pm 7.8$ | $33 \pm 8.5$ | $27 \pm 6.5$ | $23 \pm 6.8$ |
| $\delta_H = 3.5$ | $29 \pm 7.8$ | $48 \pm 13$ | $42 \pm 12$ | $40 \pm 13$ |

Table 3: Mean ± standard deviation of the SNR image generated by $\tilde{\mathbf{H}}_s^{-1}\mathbf{H}_s$

of the homography induces a complex pattern. These correlations vanish as the B-spline order grows. The mean and standard deviation of these SNR images are reported in Table 3. First of all, linear interpolation has the same mean SNR no matter the change in sampling step, as two samples only are always taken into account. In contrast, with magnification-driven models, the mean SNR grows with the downsampling factor as more samples get involved. Model $\tilde{\mathbf{H}}_1^{-1}\mathbf{H}_1$ gives a higher mean SNR than linear interpolation when $\delta_H > 1$ and an equivalent mean SNR for smaller $\delta_H$. Models $\tilde{\mathbf{H}}_3^{-1}\mathbf{H}_3$ and $\tilde{\mathbf{H}}_2^{-1}\mathbf{H}_2$ display higher mean SNR than linear interpolation for large downsampling factors and lower ones for lower downsampling factors. Understandably, the reduction presented above of the image distortions for $s > 1$ is associated with noisier images. The noise is compensated by a superior resolution resulting in SNR increases.

Regarding the evaluation of the adjoint scheme, Figure 9 compares the interpolation models for operation $\mathbf{H}_s^\top\mathbf{H}_s$ and $(\tilde{\mathbf{H}}_s^{-1})^\top\tilde{\mathbf{H}}_s^{-1}$ with $\delta_H = 2$. On the top Figure, one can see that, since linear interpolation always uses two samples no matter the magnification factor, applying $\mathbf{H}_r^\top\mathbf{H}_r$ or $(\tilde{\mathbf{H}}_r^{-1})^\top\tilde{\mathbf{H}}_r^{-1}$ to a constant image results in artificial high frequency patterns that are eliminated with our models. The model order has no impact for a constant image. Regarding noise propagation, $(\tilde{\mathbf{H}}_r^{-1})^\top\tilde{\mathbf{H}}_r^{-1}$ yields a higher SNR ($25 \pm 4.8$) than $(\tilde{\mathbf{H}}_s^{-1})^\top\tilde{\mathbf{H}}_s^{-1}$ ($20 \pm 4.5$ for $s = 1$, $20 \pm 3.5$ for $s = 2$, $19 \pm 3.6$ for $s = 3$). In all scenarios, for higher order models, the SNR images however display reduced correlation patterns. The bottom right and left Figures show two profiles taken at large wires of the resolution image for $\mathbf{H}_s^\top\mathbf{H}_s$ and $(\tilde{\mathbf{H}}_s^{-1})^\top\tilde{\mathbf{H}}_s^{-1}$. Oscillations patterns are mostly visible with schemes based on linear interpolation and are more pronounced with $\mathbf{H}_r^\top\mathbf{H}_r$. Small overshoots are noticeable at the border of the wires with $\mathbf{H}_2^\top \mathbf{H}_2$ and $\mathbf{H}_3^\top \mathbf{H}_3$ that do not appear using any model $(\tilde{\mathbf{H}}_s^{-1})^\top \tilde{\mathbf{H}}_s^{-1}$.

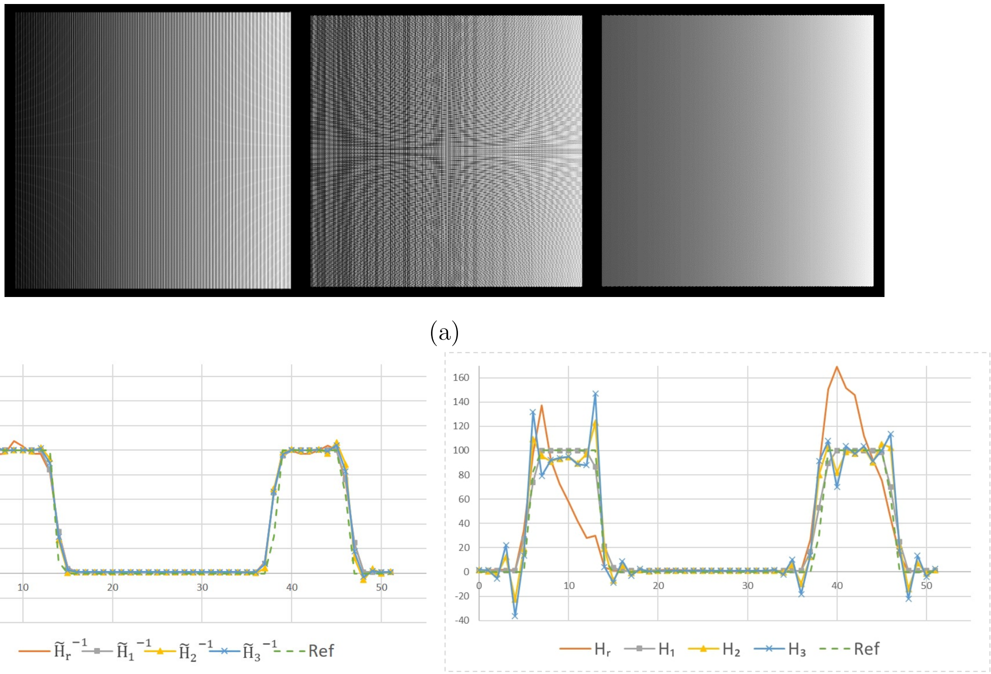

(a)

(b) (c)

Figure 9: Evaluation of direct and adjoint homography with $\delta_H = 2$. Top: uniformity (Grayscale: 0-50). From left to right: $(\tilde{\mathbf{H}}_r^{-1})^\top \tilde{\mathbf{H}}_r^{-1}$, $\mathbf{H}_r^\top \mathbf{H}_r$, others ($(\tilde{\mathbf{H}}_s^{-1})^\top \tilde{\mathbf{H}}_s^{-1}$ and $\mathbf{H}_s^\top \mathbf{H}_s$). Bottom left: plots through two large wires (dotted box of bottom left Figure 7) with $(\tilde{\mathbf{H}}_s^{-1})^\top \tilde{\mathbf{H}}_s^{-1}$. Bottom right: plots through two large wires (dotted box of bottom left Figure 7) with $\mathbf{H}_s^\top \mathbf{H}_s$.

## IV.B. Projector and backprojector

Figure 10 displays the MTF curves obtained for FDK reconstruction at iso-sampling and with $t_z = 2\alpha$ for the direct geometry. All curves were normalized to 1 at zero frequency. At iso-sampling, the MTF curves for $\mathbf{B}_r$ and $\mathbf{B}_1$ are superimposed. Just above, one can see the curves obtained with $\mathbf{B}_2$ and $\mathbf{B}_3$ that are also superimposed. When $t_z = 2\alpha$, model $\mathbf{B}_3$ outperforms $\mathbf{B}_2$ while the MTF for linear interpolation is slightly higher than that of $\mathbf{B}_1$. For the rectified geometry, $\mathbf{V}_s$ provides the same MTF as their counterparts $\mathbf{B}_s$ (curves not shown). Figure 11 displays the radial NPS curves obtained from the replicate FDK reconstructions at iso-sampling. The positive slope of these curves results from the ramp filtering. Models $\mathbf{B}_r$ and $\mathbf{B}_1$ behave similarly and correlate more the noise than higher-order models.

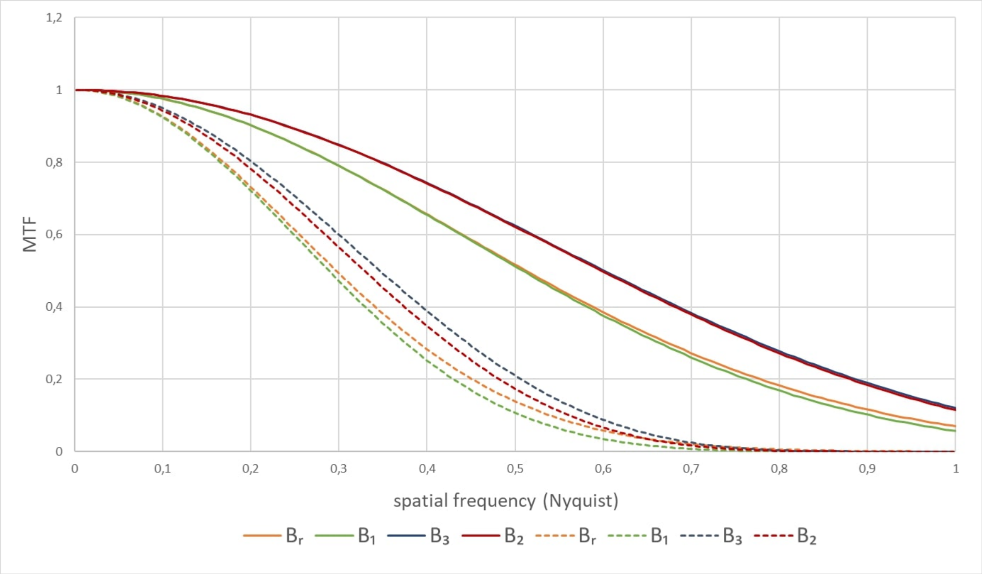

Figure 10: MTF curves obtained with $t_z = \alpha$ (solid lines) and with $t_z = 2\alpha$ (dashed lines).

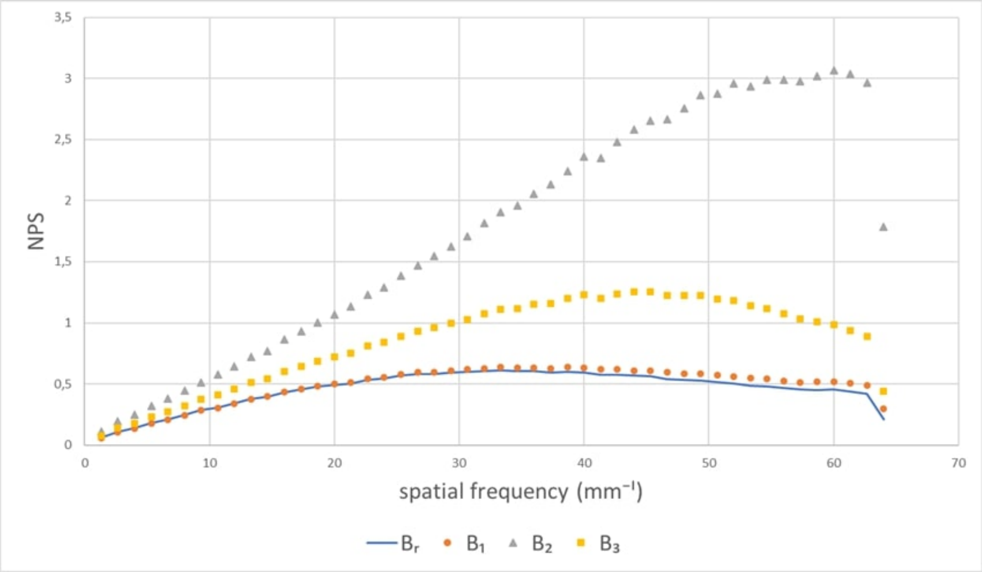

Figure 11: 1D radial NPS obtained with $t_z = \alpha$.

Figure 12 shows the SNR images obtained from $N = 200$ replicate FDK reconstructions of a uniform cylinder with $\mathbf{B}_r$ and $\mathbf{B}_s$ at iso-sampling. The window level was chosen as the mean value of each cylinder image (i.e., each mean SNR) while the window width was kept constant. Uniform SNR images are expected. We see that models $\mathbf{B}_r$ and $\mathbf{B}_1$ have similar mean SNR and display a small streak pattern, which is reduced with models $\mathbf{B}_2$ and $\mathbf{B}_3$. Model $\mathbf{B}_3$ appears as the best compromise between a uniform SNR and a high global SNR level.

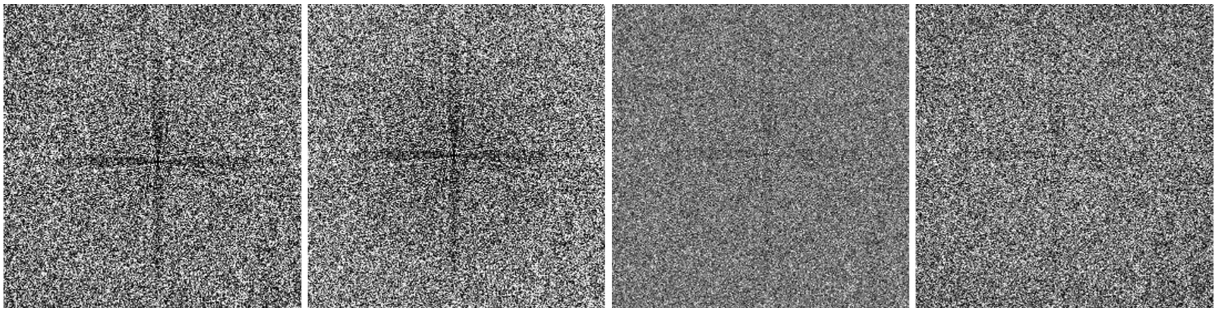

Figure 12: SNR images after FDK reconstruction of a uniform cylinder. From left to right: $\mathbf{B}_r$ (WL=128, WW=18), $\mathbf{B}_1$ (WL=122, WW=18), $\mathbf{B}_2$ (WL=63, WW=18) and $\mathbf{B}_3$ (WL=100, WW=18).

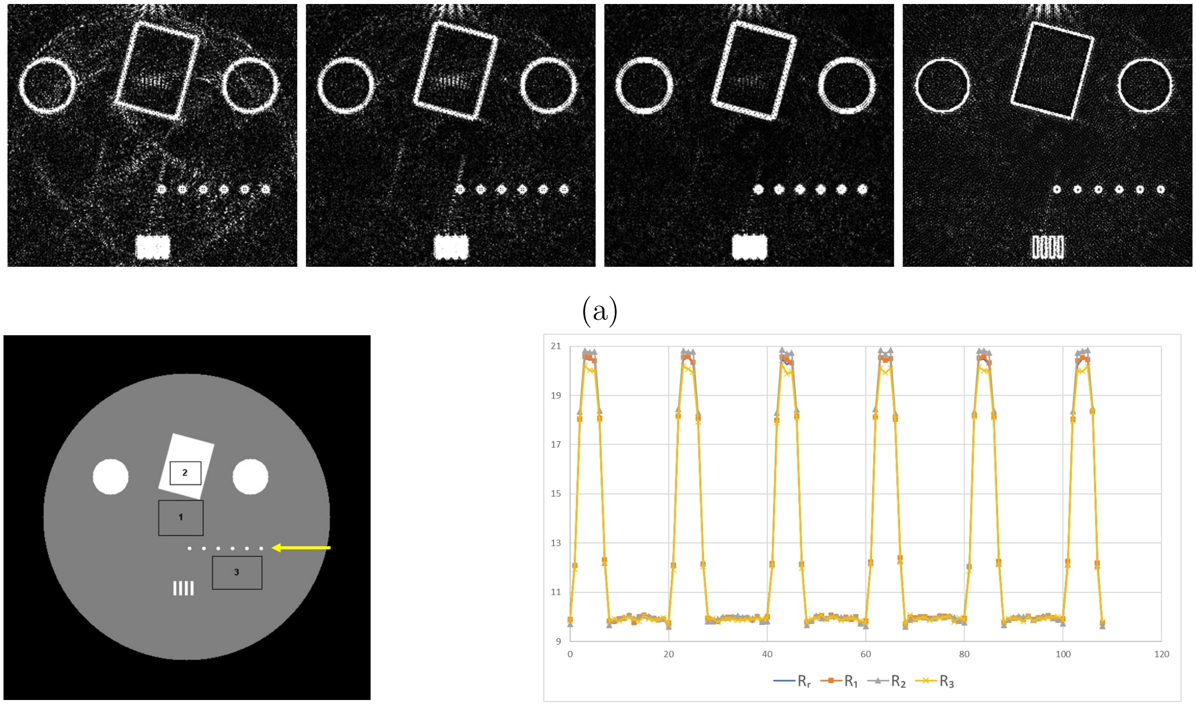

(a)

(b)

(c)

Figure 13: Iterative reconstruction of the simulated geometric phantom after 300 iterations. Top: error images between reconstructions and phantom (WL=0.15, WW=0.30) ; from left to right: $\mathbf{R}_r$, $\mathbf{R}_1$, $\mathbf{R}_2$, $\mathbf{R}_3$. Bottom left: phantom with three ROIs. Bottom right: profiles through the six wires pointed by the arrow of the bottom left Figure.

Figure 13 (top) shows a zoom on the error images between the ground truth and MBIR after 300 iterations for the central slice using projectors $\mathbf{R}_s$ and $\mathbf{R}_r$. Edge distortions and aliasing patterns are visible in all images. However they are more pronounced with $\mathbf{R}_r$. The strength of these artifacts was quantified as the mean RMSE over a union of three ROIs where they have the strongest effect. The RMSE errors are 0.74%, 0.59%, 0.56% and 0.53% of the background for projectors $\mathbf{R}_r$, $\mathbf{R}_1$, $\mathbf{R}_2$, and $\mathbf{R}_3$ respectively. Projector $\mathbf{R}_r$ yielded the highest error while projector $\mathbf{R}_3$ led to the lowest one. Plots of the horizontal profiles along the central wire are presented in Figure 13 (bottom right). Peaks have a greater intensity for $\mathbf{R}_r$, $\mathbf{R}_1$ and $\mathbf{R}_2$ than the ground truth intensity (equal to 20) while for $\mathbf{R}_3$ the intensity is correct. The iterative process inverts the discretization errors of the projector, which yields a stronger unwanted deconvolution. The profiles thus show that higher-order projectors induce less deconvolution biases, relying on a more accurate representation of the signal. This means that magnification-driven interpolation can lead to reduced edge artifacts with respect to linear interpolation.

## IV.C. Real data

Figure 14 shows the reconstructions of the bar pattern of 8 line pairs at iso-sampling and with a downsampling factor of 4. Figure 15 shows the profiles through the resolution bars according to different options and interpolation models.

All models offer similar performance when reconstructing at iso-sampling. With a downsampling of 4, the worst case is the standard approach of detector rebinning followed by linear interpolation. A first improvement is obtained by substituting the rebinning step with rectification. The highest resolution is obtained using the native geometry with $\mathbf{B}_2$ and $\mathbf{B}_3$. With $\mathbf{B}_r$, the issue of non-stationarity from peak to peak is again visible.

Table 4 shows that bin averaging of the data with $\mathbf{A}$ prior to backprojecting with linear interpolation $\mathbf{B}_r$ achieved the best noise performance, but at the price of a strong loss of resolution. Linear interpolation without bin averaging $\mathbf{B}_r$ yielded the highest noise level. In contrast, model $\mathbf{B}_1$, which led to a resolution very close to that provided by $\mathbf{B}_r$, was associated to the second lowest RMSE, that is twice lower than the RMSE obtained with $\mathbf{B}_r$. Using a first rectification homography $\mathbf{H}_s$ followed by our spline models in rectified geometry $\mathbf{V}_s$ achieved an intermediate compromise between noise and resolution for a reduced computational complexity. Using model $\mathbf{V}_3\mathbf{H}_3$ barely decreased spatial resolution compared to performing a direct reconstruction with $\mathbf{B}_3$ while gaining in noise uniformity (RMSE decrease of 20 HU).

All these observations show that the behavior of magnification-driven interpolation assessed in simulations extends to real data. Moreover, despite a non-ideal geometry, requiring a non-separable interpolation and approximate local magnifications, our approach still resulted in improvements over linear interpolation.

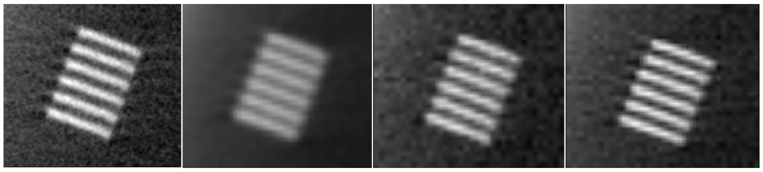

Figure 14: C-arm CBCT reconstruction of a quality assurance phantom. Displayed ROI centered on the bar pattern of 8 lp/cm (WL = 1200, WW = 2000). From left to right: $\mathbf{B}_r$ $(t_z = \alpha)$, $\mathbf{B}_r\mathbf{A}$ $(t_z = 4\alpha)$, $\mathbf{B}_r$ $(t_z = 4\alpha)$, $\mathbf{B}_3$ $(t_z = 4\alpha)$.

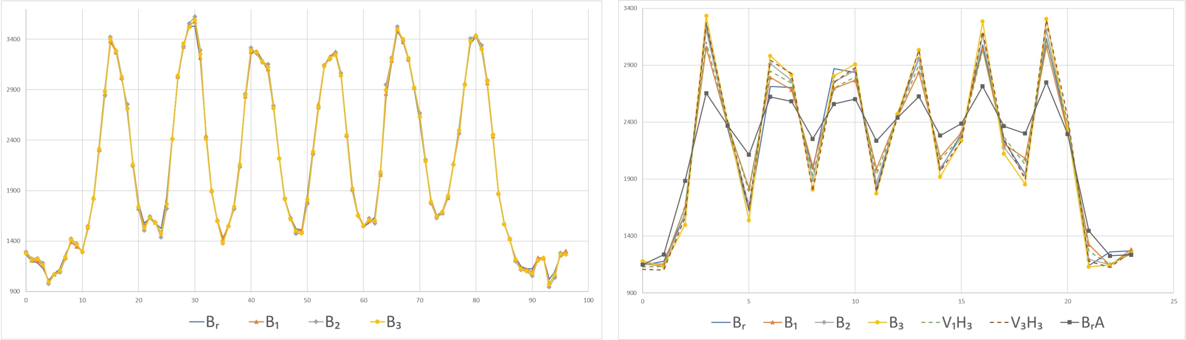

(a)

(b)

Figure 15: Profiles through the bar pattern of 8 lp/cm shown in Figure 14. Left: $t_z = \alpha$. Right: $t_z = 4\alpha$.

| $\mathbf{B}_r$ | $\mathbf{B}_1$ | $\mathbf{B}_2$ | $\mathbf{B}_3$ | $\mathbf{B}_r\mathbf{A}$ | $\mathbf{V}_1\mathbf{H}_3$ | $\mathbf{V}_3\mathbf{H}_3$ |
|---|---|---|---|---|---|---|
| 151 | 76 | 136 | 129 | 43 | 85 | 110 |

Table 4: Mean RMSE of the four uniform ROIs

## V. Discussion

The modeling of magnification, here performed through optimal expansions over B-splines of varying widths, provides a new framework for computing homographies found in flat-panel cone-beam forward and backward projections. The proposed framework generalizes current separately developed approaches of magnification-agnostic signal resampling on the one hand and geometric discretization on the other. The first approach works well-enough for common image processing tasks especially when using high-order polynomial interpolation. However, in the practice of X-ray clinical imaging, nearest neighbor (for rebinning) and linear interpolations are preferred for analytical reconstruction. The reasons are related to limited computation and storage resources and the constraint of full X-ray dose utilization, so that spatial resolution is sacrificed to noise reduction through the use of large or rebinned acquisition pixels. We here provide an array of interpolation kernels to fully benefit from small acquisition pixels with improved data resizing or rectification steps and improved projection inner steps. Our method displays reasonably simple computations through interpolation kernels of order up to 3, and enhanced noise uniformity.

We do not claim that resolution can be improved and noise decreased simultaneously: the proposed kernels may either keep the noise or blur the signal, but they do not randomly lose information, as may happen when using downsampling with a magnification-agnostic linear interpolation. At iso-sampling, the current state-of-the-art linear and DD interpolations have similar performances.

The shortcomings for the adjoint of the destination-driven projector are induced by the lack of magnification modeling in the interpolation process. The alternative approach of geometrical discretization has been introduced to overcome this issue. Again, dose and computation constraints have made the DD model a better tool for model-based iterative reconstruction than alternative classical tools of image processing. Put into our framework, we get several advantages. First, the DD appears to oscillate between linear interpolation and nearest-neighbor interpolation depending on the magnification factor, so that its preferential use is at iso-sampling. Second, its computation can be simplified through the use of the convolution of 0-order B-splines with respect to the complex logic of sorting the edges of the voxels and pixels on an intermediate axis. Third, it can be improved by slightly higher order kernels, and it can be associated to rebinning and rectification within a single modeling framework.

Improvement on clinical systems are expected from our framework. First, the increase in resolution achieved on a real acquisition of a quality assurance phantom will translate to clinical exams for linear analytical reconstruction. Secondly, regarding MBIR, let us recall that working with finer voxels than that of iso-sampling increases the computation load. Instead, a higher-order model for the volume side allows the compression of the information held by many small pixels on the detector side. We consider it an important contribution to provide an optimized link between a 0-order acquisition sampling model and a higher-order reconstruction model through either resizing or rectification, to perform reconstruction at iso-sampling. Accordingly, through the use of operators with increased symmetry, possibly based on virtual detectors where the resampled data can still be modeled as uncorrelated, our method displays features necessary for faster convergence and computation, much desirable in clinical practice.

Let us acknowledge some limitations of this work and open a few perspectives. First of all, we worked exclusively with centered B-splines of low orders, but alternative basis functions can provide additional flexibility between precision and computation load. Our results illustrate that the most straightforward choices work well in our context of C-arm CBCT. We focused on homographic transforms because they perfectly describe flat-panel detectors and have an analytical description. These transforms do not apply to the native geometry of diagnostic CT with curved detector. As we showed for the DD model, the local sampling steps can be estimated from a geometrical description and the magnification-driven interpolation is applicable. Let us add that a cone-beam geometry with a very large source to detector distance is close to parallel geometry. One should not consider that the issue of magnification vanishes in that case. This only happens when the detector is parallel to the volume. But as soon as the detector plane is not aligned with the Cartesian grid, subsampling arises and our framework is of interest to handle it.

## VI. Conclusion

A new *magnification-driven* interpolation framework is introduced for tomography. It leverages a resizing algorithm based on families of B-splines of varying widths to account for the magnifications introduced by the homographies found in flat-panel cone-beam projection. The magnifications are shown to be a key ingredient to improve the modeling of a cone-beam projector and its adjoint. A set of interpolation kernels is derived that allows novel forward and backward projection pairs. These kernels balance spatial resolution versus noise and yield better noise uniformity. The benefits with respect to linear interpolation appear more significant when downsampling frames acquired by the small pixels of X-ray flat-panel detectors: full dose usage is guaranteed, while linear interpolation randomly misses data. Magnification-driven interpolation is perfectly adapted to downsampling high-resolution data at the detector level, either through simple magnification, or through rectification that further provides simpler and faster computations. In our experiments, the tested kernels were of order up to 3. Such a choice results in reasonable computations which, by taking advantage of separability, translate well to highly-parallel computing architectures. The lowest order model turns out to reduce to the distance-driven interpolation, for which we provide new insight and computational scheme.

## Acknowledgments

This work was supported by the ANRT CIFRE Convention 2018/1587 and by the ANR research and teaching chair in Artificial Intelligence BRIDGEABLE. Emilie Chouzenoux acknowledges support from the European Research Council Starting Grant MAJORIS ERC-2019-STG-850925.

## Conflict of Interest Statement

The first three authors are full-time employees of GE Healthcare, Buc, France. Authors have no other conflicts of interest to disclose. The concepts and information presented in this article are based on research and are not commercially available. Research data are not shared.

# References

[1] J.-B. Thibault, K. Sauer, C. Bouman, and J. Hsieh, A three-dimensional statistical approach to improved image quality for multislice helical CT, Medical physics **34**, 4526–4544 (2007).

[2] H. Langet, C. Riddell, A. Reshef, Y. Trousset, A. Tenenhaus, E. Lahalle, G. Fleury, and N. Paragios, Compressed-sensing-based content-driven hierarchical reconstruction: Theory and application to C-arm cone-beam tomography, Medical Physics **42**, 5222–5237 (2015).

[3] C. Chaux, P. L. Combettes, J.-C. Pesquet, and V. R. Wajs, A variational formulation for frame based inverse problems, Inverse Problems **23**, 1495–1518 (2007).

[4] E. Chouzenoux, A. Jezierska, J.-C. Pesquet, and H. Talbot, A Majorize-Minimize subspace approach for $\ell_2 - \ell_0$ image regularization, SIAM Journal on Imaging Sciences **6**, 563–591 (2013).

[5] E. Y. Sidky, J. H. Jørgensen, and X. Pan, Convex optimization problem prototyping for image reconstruction in computed tomography with the Chambolle–Pock algorithm, Physics in Medicine and Biology **57**, 3065–3091 (2012).

[6] P. L. Combettes and J.-C. Pesquet, Proximal Splitting Methods in Signal Processing, in *Fixed-Point Algorithms for Inverse Problems in Science and Engineering*, edited by H. H. Bauschke, R. S. Burachik, P. L. Combettes, V. Elser, D. R. Luke, and H. Wolkowicz, pages 185–212, New York, 2011, Springer-Verlag.

[7] N. Komodakis and J.-C. Pesquet, Playing with Duality: An overview of recent primal-dual approaches for solving large-scale optimization problems, IEEE Signal Processing Magazine **32**, 31–54 (2015).

[8] Y. Long, J. A. Fessler, and J. M. Balter, 3D forward and back-projection for X-ray CT using separable footprints, IEEE Transactions on Medical Imaging **29**, 1839–1850 (2010).

[9] B. De Man and S. Basu, Distance-driven projection and backprojection in three dimensions, Physics in medicine and biology **49**, 2463–2475 (2004).

[10] G. L. Zeng and G. T. Gullberg, Unmatched projector/backprojector pairs in an iterative reconstruction algorithm, IEEE Transactions on Medical Imaging **19**, 548–555 (2000).

[11] R. R. Galigekere, K. Wiesent, and D. W. Holdsworth, Cone-beam reprojection using projection-matrices, IEEE Transactions on Medical Imaging **22**, 1202–1214 (2003).

[12] W. H. Press, S. A. Teukolsky, W. T. Vetterling, and B. P. Flannery, *Numerical Recipes 3rd Edition: The Art of Scientific Computing*, Cambridge University Press, USA, 3 edition, 2007.

[13] G. Zeng, Counter examples for unmatched projector/backprojector in an iterative algorithm, Chinese Journal of Academic Radiology **1**, 13–24 (2019).

[14] E. Chouzenoux, J.-C. Pesquet, C. Riddell, M. Savanier, and Y. Trousset, Convergence of proximal gradient algorithm in the presence of adjoint mismatch, Inverse Problems **37**, 065009 (2021).

[15] M. Unser, A. Aldroubi, and M. Eden, Enlargement or reduction of digital images with minimum loss of information, IEEE Transactions on Image Processing **4**, 247–258 (1995).

[16] A. Ziegler, T. Köhler, T. Nielsen, and R. Proksa, Efficient projection and backprojection scheme for spherically symmetric basis functions in divergent beam geometry, Medical Physics **33**, 4653–4663 (2006).

[17] F. Momey, L. Denis, C. Burnier-Mennessier, É. Thiébaut, J.-M. Becker, and L. Desbat, Spline driven: high accuracy projectors for tomographic reconstruction from few projections, IEEE Transactions on Image Processing **24**, 4715 – 4725 (2015).

[18] O. Faugeras, *Three-Dimensional Computer Vision: A Geometric Viewpoint*, MIT Press, Cambridge, MA, USA, 1993.

[19] Q. Luong and O. Faugeras, Self-calibration of a moving camera from point correspondences and fundamental matrices, International Journal of Computer Vision **22**, 261–289 (1997).

[20] M. Unser, A. Aldroubi, and M. Eden, Fast B-spline transforms for continuous image representation and interpolation, IEEE Transactions on Pattern Analysis and Machine Intelligence **13**, 277–285 (1991).

[21] D. G. Luenberger, *Optimization by Vector Space Methods*, John Wiley & Sons, Inc., USA, 1st edition, 1997.

[22] G. Meurant, A review on the inverse of symmetric tridiagonal and block tridiagonal matrices, SIAM J. Matrix Anal. Appl. **13**, 707–728 (1992).

[23] T. Briand and P. Monasse, Theory and practice of image B-Spline interpolation, Image Processing On Line **8**, 99–141 (2018).

[24] C. Riddell and Y. Trousset, Rectification for cone-beam projection and backprojection, IEEE Transactions on Medical Imaging **25**, 950–962 (2006).

[25] M. Unser, P. Thevenaz, and L. Yaroslavsky, Convolution-based interpolation for fast, high-quality rotation of images, IEEE Transactions on Image Processing **4**, 1371–1381 (1995).

[26] T. Briand and A. Davy, Optimization of Image B-spline Interpolation for GPU Architectures, Image Processing On Line **9**, 183–204 (2019).

[27] B. Vrcej and P. Vaidyanathan, Efficient implementation of all-digital interpolation, IEEE Transactions on Image Processing **10**, 1639–1646 (2001).

[28] M. Unser and M. Eden, FIR approximations of inverse filters and perfect reconstruction filter banks, Signal Processing **36**, 163–174 (1994).

# Appendix

Let $\theta \in \mathbb{R}$. We have

$$\xi_{\Delta}^{1,0}(\theta) = \int_{-\infty}^{+\infty} \beta_{\Delta}^{0}(\tau)\beta_{1}^{1}(\theta-\tau)d\tau = \int_{-\Delta/2}^{\Delta/2} \beta_{1}^{1}(\theta-\tau)d\tau. \tag{91}$$

- **Case I** : For $\theta \in \left[|\frac{\Delta}{2}-1|, \frac{\Delta}{2}+1\right]$, i.e., $\frac{\Delta}{2} \geq \theta - 1$, $-\frac{\Delta}{2} \leq \theta - 1$ and $\frac{\Delta}{2} \leq \theta + 1$,

$$\begin{aligned}\xi_{\Delta}^{1,0}(\theta) &= \int_{\theta-1}^{\Delta/2} (1-|\theta-\tau|)d\tau \\ &= \int_{\theta-\frac{\Delta}{2}}^{1} (1-|\tau|)d\tau. \end{aligned} \tag{92}$$

If $\theta \geq \frac{\Delta}{2}$ then

$$\begin{aligned}\xi_{\Delta}^{1,0}(\theta) &= 1 - \frac{1}{2} - \Big(\theta - \frac{\Delta}{2}\Big) + \frac{1}{2}\Big(\theta - \frac{\Delta}{2}\Big)^2 \\ &= \frac{1}{2} - \theta + \frac{\Delta}{2} + \frac{\theta^2}{2} + \frac{\Delta^2}{8} - \frac{\Delta}{2}\theta \\ &= \frac{1}{8}(\Delta^2 - 4\Delta\theta + 4\Delta + 4\theta^2 - 8\theta + 4). \end{aligned} \tag{93}$$

If $\theta \leq \frac{\Delta}{2}$ then

$$\begin{aligned}\xi_{\Delta}^{1,0}(\theta) &= \int_{\theta-\frac{\Delta}{2}}^{0}(1+\tau)d\tau + \int_{0}^{1}(1-\tau)d\tau \\ &= \frac{\Delta}{2} - \theta - \frac{1}{2}(\theta - \frac{\Delta}{2})^2 + 1 - \frac{1}{2} \\ &= \frac{1}{8}(-\Delta^2 + 4\Delta\theta + 4\Delta - 4\theta^2 - 8\theta + 4). \end{aligned} \tag{94}$$

- **Case II** : For $\theta \in \big[-1 - \frac{\Delta}{2}, -|\frac{\Delta}{2} - 1|\big]$, since $\xi_{\Delta}^{1,0}$ is an even function, its expression is deduced from Case I.

- **Case III** : For $\theta \in [1 - \frac{\Delta}{2}, \frac{\Delta}{2} - 1]$, $\frac{\Delta}{2} > 1$,

$$\xi_{\Delta}^{1,0}(\theta) = \int_{-1}^{1}(1 - |\tau|)d\tau = 1. \tag{95}$$

- **Case IV** : For $\theta \in [\frac{\Delta}{2} - 1, 1 - \frac{\Delta}{2}]$, $\frac{\Delta}{2} < 1$,

$$\xi_{\Delta}^{1,0}(\theta) = \int_{\theta-\frac{\Delta}{2}}^{\theta+\frac{\Delta}{2}}(1 - |\tau|)d\tau. \tag{96}$$

If $\theta + \frac{\Delta}{2} \leq 0$ then

$$\begin{aligned}\xi_{\Delta}^{1,0}(\theta) &= \int_{\theta-\frac{\Delta}{2}}^{\theta+\frac{\Delta}{2}}(1+\tau)d\tau \\ &= \Delta + \frac{1}{2}((\theta + \frac{\Delta}{2})^2 - (\theta - \frac{\Delta}{2})^2) \\ &= \Delta(1+\theta). \end{aligned} \tag{97}$$

If $\theta - \frac{\Delta}{2} \leq 0$ and $\theta + \frac{\Delta}{2} \geq 0$ then

$$\begin{aligned}\xi_{\Delta}^{1,0}(\theta) &= \int_{\theta-\frac{\Delta}{2}}^{0}(1+\tau)d\tau + \int_{0}^{\theta+\frac{\Delta}{2}}(1-\tau)d\tau \\ &= \frac{\Delta}{2} - \theta - \frac{1}{2}(\theta - \frac{\Delta}{2})^2 + \theta + \frac{\Delta}{2} - \frac{1}{2}(\theta + \frac{\Delta}{2})^2 \\ &= \Delta - \frac{\Delta^2}{4} - \theta^2. \end{aligned} \tag{98}$$

If $\theta - \frac{\Delta}{2} \geq 0$ then, by symmetry, we deduce the expression of $\xi_{\Delta}^{1,0}$ from (97).